

5th Institute of Physics

University of Stuttgart
Pfaffenwaldring 57
D-70569 Stuttgart

Bachelor Thesis

**Setup and Characterisation of a
Frequency-Doubled Lasersystem
for Spectroscopy of the $A^2\Sigma^+$ to
 $H^2\Sigma^+$ Transition in Nitric Oxide**

André Bisquerra

Course of Study: Physics
Examiner: Prof. Dr. Tilman Pfau
Supervisor: Dr. Harald Kübler

Commenced: April 30, 2019
Completed: Oktober 30, 2019

Abstract

English

For the trace gas sensing experiment the excitation of nitric oxide to a Rydberg state is required. The excitation is achieved by a three-photon process. In the course of this thesis, a part of the laser system for the excitation is set up using Second Harmonic Generation (SHG) and subsequently characterised. A grating stabilised diode laser is amplified by a optical fiber amplifier and frequency doubled by a Periodically Polarised Lithium Niobate (PPLN) crystal. Three methods for beam measurements of an input and output beam of a fiber coupler are performed and compared.

German

Im Rahmen dieser Arbeit soll ein optischer Aufbau zur Frequenzverdopplung realisiert und charakterisiert werden. Hierfür wird ein gitterstabilisierter Diodenlaser mit Hilfe eines Faserverstärkers verstärkt und anschließend mit einem periodisch polarisierten Lithiumniobatkristall (PPLN) frequenzverdoppelt. Der Ein- und Ausgangsstrahl eines Faserkopplers werden vermessen und verglichen. Zudem werden drei Messmethoden zur Bestimmung des Gaußschen Strahlprofils für den Ausgangsstrahl des Faserkopplers verglichen.

Contents

1	Theory	7
1.1	Wave equation and Gaussian beam	7
1.1.1	Wave equation	7
1.1.2	Paraxial approximation of the wave equation	8
1.1.3	Gaussian beam	9
1.1.4	Gaussian beam parameters	12
1.1.5	Wave matrix and q-parameter	15
1.2	Second Harmonic Generation (SHG)	17
1.2.1	Nonlinear wave equation	17
1.2.2	Mathematical description of SHG	17
1.2.3	Birefringent phase matching	20
1.2.4	Quasi phase matching	22
1.3	Stimulated emission	25
1.3.1	Atom light interaction	25
1.3.2	Mathematical description	26
2	Setup	29
2.1	Optical setup	29
2.1.1	Beam path of the setup	31
2.2	List of devices	34
2.2.1	Diode laser	34
2.2.2	Optical (fiber) amplifier	34
2.2.3	Periodically Poled Lithium Niobate (PPLN)	35
3	System Characterisation	37
3.1	Knife edge measurements	37
3.1.1	Conventional knife edge measurement	37
3.1.2	90/10 method	40
3.1.3	Chopper method	41
3.1.4	1080 nm beam at the position of the coupler for the fiber amplifier	42
3.1.5	1080 nm beam of the output of the fiber amplifier coupler	44
3.1.6	Comparison between the knife edge methods	51
4	Summary and Outlook	55
4.1	Summary	55
4.2	Outlook	57

Introduction

This thesis is part of the trace gas sensing project based on the proof of concept experiment described in [1] and [2]. The aim of the project is the investigation of a gas sensor for nitric oxide which is based on Rydberg excitations. Nitric oxide plays an important role for the immune system of the human body as explained in [3, 4, 5, 6]. In addition, an increase of the NO concentration in the breath can be a signal for breast cancer [7, 8] and inflammatory diseases like asthma [9, 10]. The detection of nitric oxide is based on a three-level excitation scheme to a Rydberg state. A Rydberg state [11] describes an excited state of an atom or molecule where the binding energy between a single valence electron and nucleus is small and thus the spatial distance large. This allows the ionisation of the molecule caused by collisions with the background gas. The excitation scheme and principle of measurement is described in the masters thesis of Fabian Munkes [12] which was aimed on the investigation of the first transition of the three-photon process.

This thesis focuses on the second transition taking place at 540 nm. A diode laser in the infrared region is used due to the lack of laser diodes at the region around 540 nm and amplified using an optical fiber amplifier. A Periodically Poled Lithium Niobate (PPLN) is then used for Second Harmonic Generation (SHG) to obtain the desired wavelength. The concept of frequency doubling can be employed to obtain 540 nm from a 1080 nm laser. This process is called SHG and is based on nonlinear effects in an optical medium [13]. The effect is well known and optimized for the application in the laboratory [14].

In the course of this thesis, a setup for the generation of a second harmonic should be realised, characterised and documented. A grating stabilised diode laser of wavelength $\lambda = 1080$ nm is used as seed laser and amplified by an optical fiber amplifier. The wide collimated high power beam is then focused and aligned onto a Periodically Polarised Lithium Niobate (PPLN) crystal for Second Harmonic Generation. The generated beam of wavelength $\lambda = 540$ nm is then extracted and diverted to another setup for spectroscopy of the $A^2\Sigma^+$ to $H^2\Sigma^+$ transition of Nitric Oxide.

Due to a technical defect on the fiber amplifier, the main characterisation of the system couldn't be carried out. Instead the coupling efficiency for the fiber leading to the fiber amplifier and the corresponding input and output beams are analysed instead with three methods for comparison.

The first chapter of this thesis contains the theoretical basics necessary for the understanding and the built up of the optical setup. This includes the Gaussian beam optics as well as SHG and stimulated emission.

The second chapter focuses on the setup itself. It contains a schematic of the optical setup with all of its components and their specifications. The beam path including all characteristics and alterations is also described.

The third chapter contains the actual measurements of the Gaussian beam regarding the input and output of a self-built fiber coupler leading to the fiber amplifier.

1 Theory

The theoretical basics for the functionality of the used devices and for the methods used for the setup to achieve proper results are described in this chapter.

1.1 Wave equation and Gaussian beam

The derivation of the linear wave equation, paraxial approximation and general description of the Gaussian beam are described in [15] and this section follows closely.

1.1.1 Wave equation

The wave equation can be derived from Maxwell's equations (1.1) by using the rotational operator twice on the electric field as shown in (1.2) and setting the electric current density to $\vec{j} = 0$.

$$\begin{aligned}\nabla \cdot \vec{D} &= \rho \\ \nabla \cdot \vec{B} &= 0 \\ \nabla \times \vec{E} &= -\partial_t \vec{B} \\ \nabla \times \vec{H} &= \vec{j} + \partial_t \vec{D}\end{aligned}\tag{1.1}$$

With the displacement field \vec{D} , the magnetic field \vec{B} , the electric field \vec{E} , the magnetizing field \vec{H} and the charge density ρ .

$$\begin{aligned}\nabla \times (\nabla \times \vec{E}) &= \nabla \times (-\partial_t \vec{B}) \\ \nabla (\nabla \cdot \vec{E}) - \Delta \vec{E} &= -\partial_t (\nabla \times \vec{B}) = -\partial_t \mu_0 \mu (\nabla \times \vec{H}) \\ \Delta \vec{E} &= \mu_0 \mu \partial_t^2 \vec{D},\end{aligned}\tag{1.2}$$

with the vacuum permittivity μ_0 , the relative permittivity μ and the Laplacian operator in spatial coordinates:

$$\Delta = \frac{\partial^2}{\partial x^2} + \frac{\partial^2}{\partial y^2} + \frac{\partial^2}{\partial z^2}\tag{1.3}$$

The left hand side of (1.2) is evaluated by a mathematical relation of the cross product. The right hand side is derived by using Maxwell's equations (1.1) and the linear electric displacement field \vec{D} :

$$\vec{D} = \epsilon_0 \epsilon \vec{E}\tag{1.4}$$

with the relative permeability ϵ and the relation between the magnetic field density \vec{H} and the magnetic flux density \vec{B} :

$$\vec{B} = \mu_0 \mu \vec{H}$$

This results in

$$\Delta \vec{E} = \mu_0 \mu \epsilon_0 \epsilon \partial_t^2 \vec{E} = \frac{n^2}{c^2} \partial_t^2 \vec{E}, \quad (1.5)$$

with the speed of light in vacuum:

$$c = \sqrt{\epsilon_0 \mu_0}^{-1}, \quad (1.6)$$

and the refractive index

$$n = \sqrt{\mu \epsilon}. \quad (1.7)$$

The wave equation describes the correlation between spatial and temporal change of a wave and is a second-order linear partial differential equation.

The wave equation can be simplified by evaluating the time-dependent part of the equation using an arbitrary function $\vec{E}(\vec{r}, t) = \vec{E}(\vec{r}) \cdot e^{-i\omega t}$ that is not attenuated by time t . ω is the angular frequency.

$$\begin{aligned} \Delta \vec{E}(\vec{r}) \cdot e^{-i\omega t} &= \frac{n^2}{c^2} \frac{\partial^2}{\partial t^2} \vec{E}(\vec{r}) \cdot e^{-i\omega t} \\ &= -\frac{\omega^2 n^2}{c^2} \vec{E}(\vec{r}) \cdot e^{-i\omega t} \\ \Delta \vec{E}(\vec{r}) &= -\frac{\omega^2 n^2}{c^2} \vec{E}(\vec{r}) \end{aligned}$$

With the relation of the wave vector $k = \frac{\omega n}{c}$ in a material of refractive index n the Helmholtz equation emerges:

$$0 = \Delta \vec{E}(\vec{r}) + k^2 \vec{E}(\vec{r}) \quad (1.8)$$

1.1.2 Paraxial approximation of the wave equation

The paraxial wave equation describes the propagation of a wave regarding a small angle between the propagation axis of the wave and the optical axis. Using a combination of transversal amplitude function $\vec{A}(\vec{r})$ that only changes slightly regarding z and a planar wave as in (1.9).

$$\vec{E}(\vec{r}) = \vec{A}(\vec{r}) \cdot e^{ikz}. \quad (1.9)$$

The amplitude function is only allowed to change slightly regarding the propagation in z -direction.

$$\delta A = \left(\frac{\partial A}{\partial z} \right) \delta z = \left(\frac{\partial A}{\partial z} \right) \lambda \ll A,$$

λ being the characteristic length. Approximating this result yields

$$\left(\frac{\partial A}{\partial z}\right) \ll \frac{A}{\lambda} = \frac{kA}{2\pi} \approx kA$$

and calculating the second derivative:

$$\left(\frac{\partial^2 A}{\partial z^2}\right) \ll \frac{\partial}{\partial z}(kA) = k \left(\frac{\partial A}{\partial z}\right) \approx k^2 A.$$

This leaves

$$\frac{\partial^2 A}{\partial z^2} \ll k \frac{\partial A}{\partial z}.$$

Inserting the approach (1.9) into the Helmholtz equation (1.8) and separating z - from transversal derivations yields the paraxial wave equation:

$$\begin{aligned} 0 &= \Delta \vec{E}(\vec{r}) + k^2 \vec{E}(\vec{r}) \\ &= \Delta \vec{A}(\vec{r}) \cdot e^{ikz} + k^2 \vec{A}(\vec{r}) \cdot e^{ikz} \\ &= \Delta_T \vec{A}(\vec{r}) - 2ik \frac{\partial}{\partial z} \vec{A}(\vec{r}). \end{aligned} \quad (1.10)$$

1.1.3 Gaussian beam

The Gaussian beam is a suitable concept of paraxial optics to describe light propagation of a monochromatic source.

Using the same approach as for the linear wave equation (1.5) itself, the Gaussian beam can be derived from a spherical wave (1.11). The Gaussian beam is a solution of the paraxial wave equation (1.10).

$$\vec{E}(\vec{r}) = \frac{E_0}{|\vec{r}|} \cdot e^{-ik\vec{r}}. \quad (1.11)$$

Using a spherical wave (1.11) as a starting point and the paraxial approximation where the radial change of the amplitude function is smaller than the change on the optical axis:

$$x^2 + y^2 \ll z^2. \quad (1.12)$$

The Cartesian coordinates are given by $r = (x, y, z)^T$. Rearranging the term and approximating the square root of $\frac{x^2+y^2}{z^2} \approx 0$ in the far field results in

$$\begin{aligned} |\vec{r}| &= \sqrt{x^2 + y^2 + z^2} = z \cdot \sqrt{1 + \frac{x^2 + y^2}{z^2}} \\ &\approx z \cdot \left[1 + \frac{x^2 + y^2}{2z^2} - \mathcal{O}\left(\frac{1}{z^4}\right) \right] = z + \frac{x^2 + y^2}{2z} + \mathcal{O}\left(\frac{1}{z^3}\right). \end{aligned} \quad (1.13)$$

This can be approximated by using condition (1.12) for linear proportionality:

$$z + \frac{x^2 + y^2}{2z} \approx z \quad (1.14)$$

Evaluating the spherical wave equation (1.11) by applying the approximations (1.13) and (1.14) yields:

$$\begin{aligned} \vec{E}(\vec{r}) &= \frac{E_0}{|\vec{r}|} \cdot e^{-ik\vec{r}} \\ &\approx \frac{E_0}{\left(z + \frac{x^2 + y^2}{2z}\right)} \cdot e^{-ik\left(z + \frac{x^2 + y^2}{2z}\right)} \\ &\approx \frac{E_0}{z} \cdot e^{-ikz} \cdot e^{-ik\frac{x^2 + y^2}{2z}} \\ &= \vec{A}(\vec{r}) \cdot e^{-ikz}, \end{aligned}$$

where $\vec{A}(\vec{r})$ is the amplitude function:

$$\vec{A}(\vec{r}) = \frac{E_0}{z} \cdot e^{ik\frac{x^2 + y^2}{2z}}.$$

If $\vec{E}(\vec{r})$ is a solution of the paraxial wave equation, a shift $z \rightarrow z + \tilde{z}$ is also a solution even if $\tilde{z} = iz_R$ is a complex value $\tilde{z} \in \mathbb{C}$.

$$\vec{E}(\vec{r}) = \frac{E_0}{z + iz_R} \cdot e^{-ik\frac{\rho^2}{2(z+iz_R)}} \cdot e^{-ik(z+iz_R)} \quad (1.15)$$

$$= \frac{E_0}{q(z)} \cdot e^{-ik\frac{\rho^2}{2q(z)}} \cdot e^{-ik q(z)}, \quad (1.16)$$

where $q(z) = z + iz_R$ is the q -parameter and z_R the Rayleigh length as explained in 1.1.4. Separating real and imaginary part of the inverse q -parameter $\frac{1}{q(z)}$ through complex conjugated expansion and rearranging terms then allows to write

$$\begin{aligned} \frac{1}{q(z)} &= \frac{1}{z + iz_R} && \left| \begin{array}{l} z - iz_R \\ z - iz_R \end{array} \right. \\ &= \frac{z - iz_R}{z^2 + z_R^2} = \frac{z}{z^2 + z_R^2} - i \frac{z_R}{z^2 + z_R^2} \\ &= \frac{1}{z \left(1 + \left(\frac{z_R}{z}\right)^2\right)} - i \frac{1}{z_R \left(1 + \left(\frac{z}{z_R}\right)^2\right)}. \end{aligned}$$

The following definitions are applied:

$$R(z) = z \left(1 + \left(\frac{z_R}{z}\right)^2\right), \quad (1.17)$$

representing the radial curvature of the Gaussian beam and

$$\omega(z) = \omega_0 \sqrt{1 + \left(\frac{z}{z_R}\right)^2}, \quad (1.18)$$

the Gaussian beam waist function with the relation of the beam waist ω_0 , the wavelength λ and the Rayleigh length z_R :

$$\omega_0 = \sqrt{\frac{\lambda z_R}{\pi}}, \quad (1.19)$$

as explained and visualized in section 1.1.4. The inverse q -parameter can therefore be described as:

$$\frac{1}{q(z)} = \frac{1}{R(z)} - i \frac{\lambda}{\pi \omega(z)^2}.$$

Taking all previous calculations and approximations into account, the Gaussian beam can be described by:

$$\vec{E}(\vec{r}) = \frac{E_0}{z + iz_R} \cdot e^{-ik \frac{\rho^2}{2R(z)}} \cdot e^{-\frac{\rho^2}{\omega(z)^2}} \cdot e^{-ikz} \cdot e^{kz_R}.$$

This yields an amplitude in the focus $x = y = z = 0$ of the beam of:

$$\vec{E}(z = 0, \rho = 0) = \frac{E_0}{iz_R} \cdot e^{kz_R}.$$

For normalization, the previous equation is multiplied by a factor,

$$iz_R \cdot e^{-kz_R},$$

as introduced in [16], which results in:

$$\vec{E}(\vec{r}) = E_0 \frac{iz_R}{z + iz_R} \cdot e^{-ik \frac{\rho^2}{2R(z)}} \cdot e^{-\frac{\rho^2}{\omega(z)^2}} \cdot e^{-ikz}. \quad (1.20)$$

A further simplification can be achieved by applying the general complex relation between Cartesian and polar coordinates

$$z = a + ib = r \cdot e^{i\phi}, \quad (1.21)$$

where:

$$\begin{aligned} r &= \sqrt{a^2 + b^2}, \\ \phi &= \arctan\left(\frac{b}{a}\right). \end{aligned} \quad (1.22)$$

Therefore equation (1.20) can be rewritten as:

$$\vec{E}(\vec{r}) \propto \frac{i}{z + iz_R} = \frac{1}{\sqrt{z^2 + z_R^2}} e^{i \arctan\left(\frac{z}{z_R}\right)}.$$

Using the relation of the Gaussian beam waist (1.18) and the definition of the Gouy phase $\xi(z) = \arctan\left(\frac{z}{z_R}\right)$ results in the well known Gaussian beam equation:

$$\vec{E}(\vec{r}) = E_0 \cdot \frac{\omega_0}{\omega(z)} \cdot e^{-ik \frac{\rho^2}{2R(z)}} \cdot e^{-\frac{\rho^2}{\omega(z)^2}} \cdot e^{-i(kz - \xi(z))}. \quad (1.23)$$

1.1.4 Gaussian beam parameters

There are only two values needed for the description of a Gaussian beam, the wavelength λ and the Rayleigh range z_R . A third value might be needed to describe a Gaussian beam with a shift z_0 of the focus regarding $z = 0$. The Rayleigh range z_R is defined as the distance from the focus where the waist corresponds to:

$$\omega(z_R) = \sqrt{2}\omega_0,$$

or the transversal area of the beam:

$$A(z_R) = 2A_0,$$

where A_0 is the beam area at the focal point and ω_0 the half width of the Gaussian beam at the focal point and defines the width of the beam where the intensity falls down to I_0/e^2 of the maximum intensity I_0 . The confocal parameter b is defined by the distance between both Rayleigh points and therefore:

$$b = 2z_R$$

The focal waist ω_0 , the wavenumber k and the divergence angle θ_0 can be calculated by the following relations:

$$\omega_0 = \sqrt{\frac{\lambda z_R}{\pi}}, \quad (1.19)$$

$$k = \frac{2\pi}{\lambda},$$

$$\theta_0 = \frac{\lambda}{\pi\omega_0}. \quad (1.24)$$

The beam divergence angle θ describes the collimation of the beam and is applicable in the far field where $z \gg z_R$. The Gaussian beam waist along the optical axis can be described by

$$\omega(z) = \omega_0 \sqrt{1 + \left(\frac{z}{z_R}\right)^2} \quad (1.18)$$

and its radial component is depicted in figure 1.1. The waist can be different regarding the radial plane which results in an elliptical Gaussian beam profile. The radial phase (1.25) describes the course of phase in radial direction from the focus of the beam as shown in figure 1.2.

$$\vec{E}(\rho, R(z)) = e^{\frac{ik\rho^2}{R(z)}}, \quad (1.25)$$

with

$$R(z) = z \left(1 + \left(\frac{z_R}{z}\right)^2 \right), \quad (1.17)$$

describing the radial curvature of the wavefront as depicted in figure 1.3.

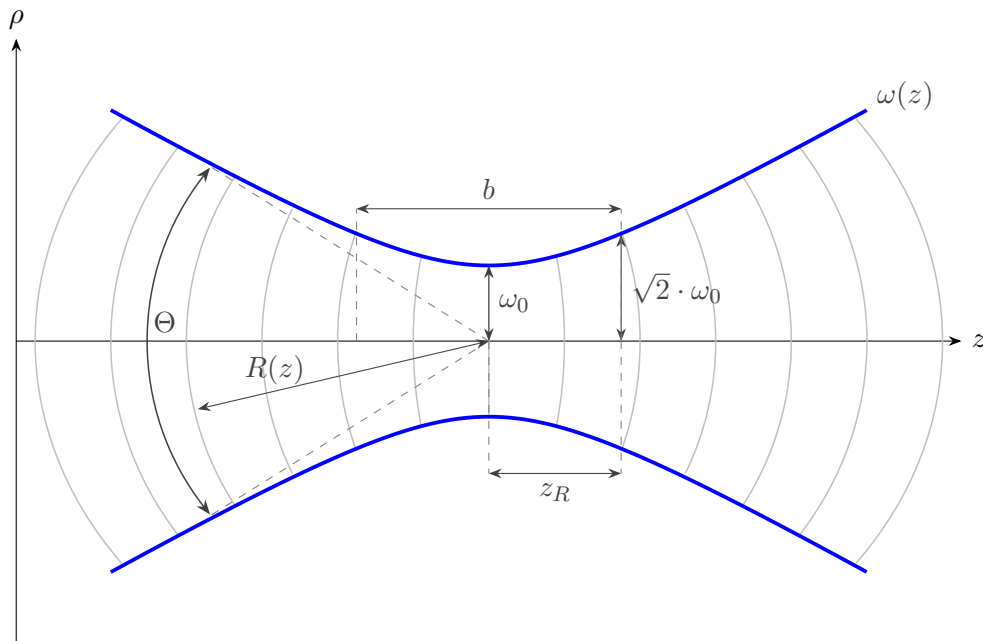


Figure 1.1: Schematic waist $\omega(z)$ of a Gaussian beam propagating along the optical z -axis with Rayleigh length z_R , confocal parameter b , curvature $R(z)$ and divergence angle θ .

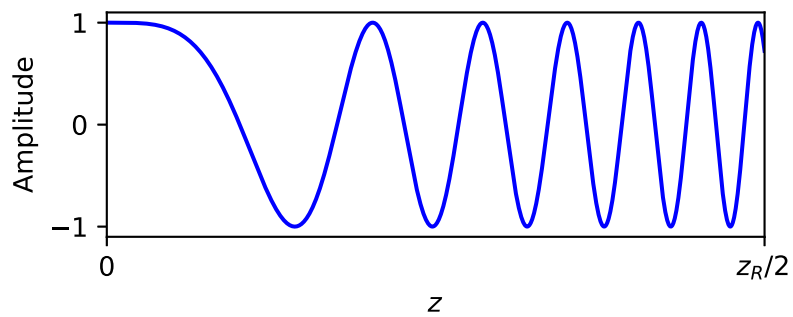


Figure 1.2: Radial phase of the Gaussian beam dependent on the position along the optical z -axis.

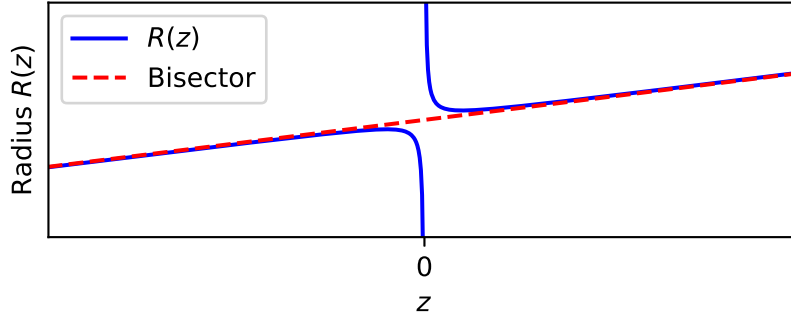


Figure 1.3: Radius of the Gaussian beam dependent on the position along the optical z -axis.

The radius of the wave front regarding the focal point is $\pm\infty$ in the focal point and rises proportionally to z in the far field as shown in figure 1.2. The Gouy Phase (1.27) describes the change in phase a Gaussian beam experiences by passing its focal point.

$$\vec{E}(z, \xi(z)) = e^{i(kz - \xi(z))} \quad (1.26)$$

with the Gouy phase:

$$\xi(z) = \arctan\left(\frac{z}{z_R}\right). \quad (1.27)$$

The additional phase of π is constantly added to the transversal phase kz . 90% of the phase shift is added within the range of $13 \cdot z_R$. This also adds a shift in the $-\infty$ range of $-\frac{\pi}{2}$ and in ∞ a shift of $\frac{\pi}{2}$ compared to a planar wave. The comparison between a planar wave with and without Gouy phase is depicted in figure 1.4. The intensity distribution of the Gaussian

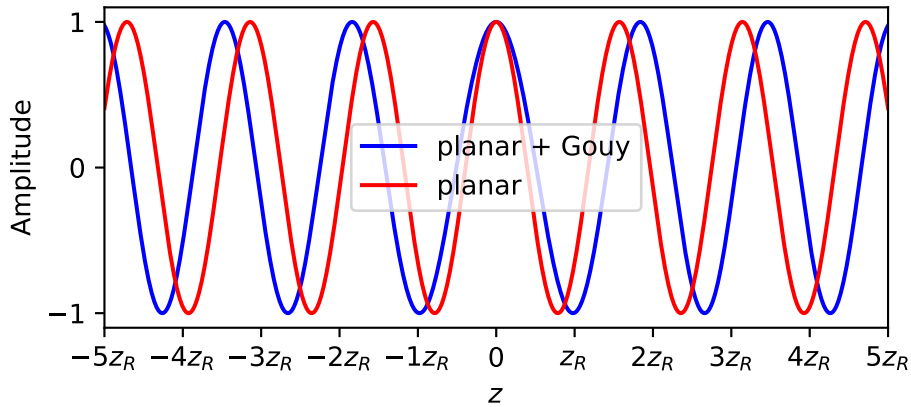


Figure 1.4: Phase of the Gaussian beam experiencing a shift in the range of the focus caused by the Gouy phase.

beam of the transversal electromagnetic field can be calculated by (1.28) and corresponds to a Gaussian shape as depicted in 1.5.

$$I(\rho) = |E(\rho)|^2 = I_0 e^{-\frac{2\rho^2}{\omega^2}} \quad (1.28)$$

The intensity distribution along the optical axis as in (1.29) corresponds to a Lorentzian shape as depicted in 1.5.

$$\begin{aligned} I(z) &= |E(z)|^2 = I_0 \frac{\omega_0^2}{\omega(z)^2} \\ &= \frac{I_0}{1 + \left(\frac{z}{z_R}\right)^2} \end{aligned} \quad (1.29)$$

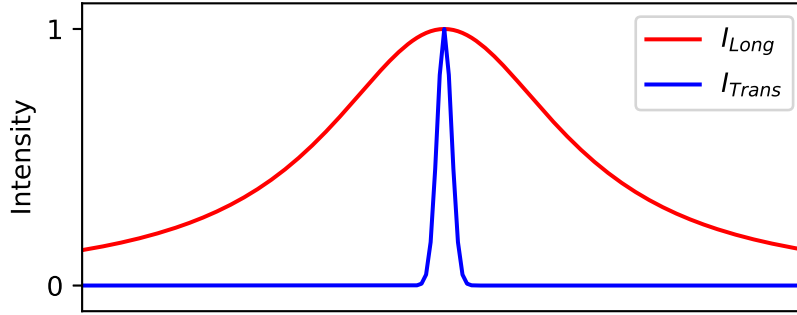


Figure 1.5: The transversal and longitudinal intensity distribution of a Gaussian beam where the width of the transversal intensity distribution has been expanded for presentation purposes.

1.1.5 Wave matrix and q-parameter

The q -parameter contains all information about the Gaussian beam:

$$q(z) = z + i \frac{\omega_0^2 \pi}{\lambda}.$$

The simple ABCD-Matrix propagation formalism of ray optics can be used to describe the propagation of a Gaussian beam in a system of optics. Similar to the ABCD matrices, propagation M_p and translation M_t matrices can be defined:

$$M_p = \begin{pmatrix} 1 & d \\ 0 & 1 \end{pmatrix}, \quad M_t = \begin{pmatrix} 1 & 0 \\ -\frac{1}{f} & 1 \end{pmatrix}.$$

In this example, M_p is a matrix for propagation distance d in a medium of refractive index n and M_t is a translation matrix for a thin lens of focal length f .

A system of multiple optics can be described by multiplying these matrices in reversed order to the propagation direction:

$$M_{\text{system}} = \begin{pmatrix} A & B \\ C & D \end{pmatrix} = M_3 \cdot M_2 \cdot M_1.$$

In contrast to the ray optics, where a ray can be defined through a vector containing the angle between propagation and optical axis as well as propagation length and simply multiplied with the system matrix M_{system} , the q -parameter can be obtained by the following relation:

$$q_2 = \frac{A \cdot q_1 + B}{C \cdot q_1 + D},$$

where q_1 is the q -parameter parameter at the Gaussian beam in front of the optical system, A to D are the entries of the matrix M_{system} and q_2 describes the Gaussian beam altered by the optical system.

1.2 Second Harmonic Generation (SHG)

A general description of the following sections covering the nonlinear wave equation, second harmonic generation and its optimisation conditions can be found in [17]. The basic derivation for the second harmonic generation has been used for this elaboration.

1.2.1 Nonlinear wave equation

The linear wave equation (1.5) applies to a non-dielectric material only. A dielectric material consists of bound charges (atomic nuclei and electrons) that are slightly separated by the presence of an external electric field \vec{E} . The separation of charges induces an electric dipole moment \vec{p} :

$$\vec{p} = q \cdot \vec{d},$$

where \vec{d} is the distance vector of the charges q of the bound pair. The polarisation \vec{P} is given by the sum of the electric dipole moments:

$$\vec{P} = \sum_i \vec{p}_i.$$

The electric displacement field \vec{D} for dielectric material is defined as:

$$\vec{D} = \epsilon_0 \vec{E} + \vec{P}_{NL} = \epsilon_0 \vec{E} + \epsilon_0 \sum_n \chi^{(n)} \vec{E}^n, \quad (1.30)$$

where \vec{E} is the external applied field, ϵ_0 the permeability in vacuum, $\chi^{(n)}$ the susceptibility and \vec{P} is the polarisation of the material.

Using (1.30) with the same approach as in (1.2) for deriving the linear wave equation results in the wave equation for a nonlinear material:

$$\Delta \vec{E} - \frac{n^2}{c^2} \partial_t^2 \vec{E} = \mu_0 \mu \partial_t^2 \vec{P}_{NL}, \quad (1.31)$$

with the refractive index n , the permittivity μ_0 in vacuum and the relative permittivity μ .

1.2.2 Mathematical description of SHG

Frequencies other than ω_1 and ω_2 where $\omega_2 = 2\omega_1$ are neglected in the following calculations. For simplification, the total electric field inside the material is considered to propagate along the optical z -axis only and is composed by the electric fields of frequencies ω_1 and ω_2 :

$$E(z, t) = E^{\omega_1}(z, t) + E^{\omega_2}(z, t), \quad (1.32)$$

where the electric field component of one frequency is described by:

$$E^{\omega_j}(z, t) = \frac{1}{2} \left(A_j(z) e^{-i(\omega_j t - k_j z)} + c.c. \right), \quad (1.33)$$

with the amplitude function $A(z)$ and the complex conjugate (*c.c.*). The second order nonlinear polarisation of the crystal is given by:

$$P_{NL}^{(2)} = \epsilon_0 \chi^{(2)} \vec{E}(z, t)^2. \quad (1.34)$$

Using (1.32) and (1.33) to evaluate the second order susceptibility $\chi^{(2)}$ of the nonlinear polarisation (1.34) using the relation:

$$A_i A_i^* = A_i^* A_i,$$

yields:

$$\begin{aligned} P_{NL} = & \frac{\epsilon_0}{4} \chi^{(2)} \left(A_1(z)^2 e^{-2i(\omega_1 t - k_1 z)} + A_1^*(z)^2 e^{2i(\omega_1 t - k_1 z)} + A_2(z)^2 e^{-2i(\omega_2 t - k_2 z)} \right. \\ & + A_2^*(z)^2 e^{2i(\omega_2 t - k_2 z)} + 2A_1(z)A_1^*(z) + 2A_2(z)A_2^*(z) \\ & + 2A_1(z)A_2(z)e^{-i((\omega_1 + \omega_2)t - (k_1 + k_2)z)} + 2A_1^*(z)A_2^*(z)e^{i((\omega_1 + \omega_2)t - (k_1 + k_2)z)} \\ & \left. + 2A_1(z)A_2^*(z)e^{-i((\omega_1 - \omega_2)t - (k_1 - k_2)z)} + 2A_1^*(z)A_2(z)e^{i((\omega_1 - \omega_2)t - (k_1 - k_2)z)} \right). \end{aligned}$$

First order polarisation as well as terms of the second order, not relating frequency and frequency amplitude of both components ω_1 and ω_2 are omitted in further calculations.

Separating the two terms leaves:

$$P_{NL}(\omega_1) = \frac{1}{2} \epsilon_0 \chi^{(2)} \left(A_1(z)A_2^*(z)e^{-i(\omega_1 t - (k_1 - k_2)z)} + c.c. \right), \quad (1.35)$$

$$P_{NL}(\omega_2) = \frac{1}{4} \epsilon_0 \chi^{(2)} \left(A_1(z)A_1(z)e^{-i(\omega_2 t - 2k_1 z)} + c.c. \right). \quad (1.36)$$

$P_{NL}(\omega_2)$ describes the polarisation oscillating at the frequency $2\omega_1 = \omega_2$ dependent on the local amplitude function of the external field while $P_{NL}(\omega_1)$ describes the polarisation oscillating at ω_1 dependent on the correlation of the amplitude function of both electric fields.

Assuming each frequency (1.33) obeys the nonlinear driven wave equation (1.31): yields:

$$\left[\left(\frac{\omega_1^2 n(\omega_1)^2}{c^2} - k_1^2 \right) \frac{A_1}{2} - ik_1 \frac{dA_1}{dz} \right] e^{-i(\omega_1 t - k_1 z)} + c.c. = \mu_0 \mu \partial_t^2 P_{NL}(\omega_1), \quad (1.37)$$

$$\left[\left(\frac{\omega_2^2 n(\omega_2)^2}{c^2} - k_1^2 \right) \frac{A_2}{2} - ik_2 \frac{dA_2}{dz} \right] e^{-i(\omega_2 t - k_2 z)} + c.c. = \mu_0 \mu \partial_t^2 P_{NL}(\omega_2). \quad (1.38)$$

Neglecting the nonlinear polarisation in the coupled wave equations (1.37) and (1.38) results in the definition of the wave vector \vec{k} for both waves:

$$\begin{aligned} \frac{\omega_1^2 n(\omega_1)^2}{c^2} - k_1^2 &= 0 \\ \frac{\omega_2^2 n(\omega_2)^2}{c^2} - k_2^2 &= 0 \end{aligned}$$

Using (1.36), the coupled wave equation (1.38) and assuming that $\mu \approx 1$ while neglecting complex conjugates results in:

$$-ik_2 \frac{dA_2}{dz} e^{-i(\omega_2 t - k_2 z)} = \partial_t^2 \frac{\mu_0 \epsilon_0}{4} \chi^{(2)} A_1(z)A_1(z)e^{-i(\omega_2 t - 2k_1 z)}.$$

With the speed of light (1.6) and the refractive index (1.7) follows:

$$\frac{dA_1}{dz} = -\frac{i\omega_1^2}{k_1 c^2} \frac{\chi^{(2)}}{2} A_1(z) A_2^*(z) e^{i(k_2 - 2k_1)z} + c.c. \quad (1.39)$$

$$\frac{dA_2}{dz} = -\frac{i\omega_2^2}{k_2 c^2} \frac{\chi^{(2)}}{4} A_1(z) A_1(z) e^{-i(k_2 - 2k_1)z} + c.c. \quad (1.40)$$

$$= -\frac{i\omega_1^2}{k_1 c^2} \frac{\chi^{(2)}}{2} A_1(z) A_1(z) e^{-i(k_2 - 2k_1)z} + c.c. \quad (1.41)$$

Assuming the fundamental wave is not to be depleted within the crystal as in [16], the amplitude function can be described as:

$$A_1(z) = \alpha_1 - \beta_1 e^{-i\Delta k z},$$

where

$$\Delta k = k_2 - 2k_1, \quad (1.42)$$

and

$$\beta_1 = \frac{\omega_1^2}{k_1 \Delta k} \frac{\chi^{(2)}}{2c^2} A_1(z) A_1(z).$$

α can be determined from the boundary condition:

$$\begin{aligned} A_2(z=0) &= \alpha_2 - \beta_2 = 0 \\ \Rightarrow \alpha_2 &= \beta_2. \end{aligned}$$

The amplitude function yields:

$$A_2(z) = \frac{\omega_1^2}{k_1 \Delta k c^2} \frac{\chi^{(2)}}{2} \left(1 - e^{-i\Delta k z}\right) A_1(z) A_1(z) \quad (1.43)$$

The amplitude function (1.43) of the frequency component ω_2 can now be used to calculate the intensity $I_2(z)$ regarding the position z along the optical axis:

$$\begin{aligned} I_2(z) &= \frac{1}{2} c \epsilon_0 |A_2(z)|^2 \\ &= \frac{1}{2} c \epsilon_0 \left(\frac{\omega_1^2}{k_1 \Delta k c^2} \frac{\chi^{(2)}}{2} \right)^2 I_1^2 \left| 1 - e^{-i\Delta k z} \right|^2. \end{aligned}$$

Rearranging and using the relation from [18] then results in:

$$\sin(x) = \frac{1}{2i} \left(e^{ix} - e^{-ix} \right),$$

the intensity distribution can be described by:

$$I_2(z) = \frac{1}{2} \frac{\epsilon_0}{c} \left(\frac{\omega_1 \chi^{(2)}}{2n(\omega_1)} \right)^2 \cdot I_1^2 \cdot \frac{\sin^2\left(\frac{1}{2}\Delta k z\right)}{\left(\frac{1}{2}\Delta k z\right)^2} \cdot z^2, \quad (1.44)$$

with the critical value $\Delta k = k_2 - 2k_1$.

The waves with different wave velocity result in a modulation of $I_2(z)$ with period $2l_c$ as depicted in figure 1.6. The coherence length l_c describes the length that can efficiently participate in SHG before generated photons of different phase start to interfere destructively.

$$l_c = \frac{\pi}{\Delta k} = \frac{\pi}{k_2 - 2k_1} = \frac{\frac{\lambda}{2}}{n(\omega_2) - n(\omega_1)}, \quad (1.45)$$

with the following relation for the refractive index:

$$k = \frac{\omega n(\omega)}{c} = \frac{2\pi n(\omega)}{\lambda}.$$

Approximating equation (1.44) for optimal phase matching $\Delta k = 0$ yields:

$$I_2(z, \Delta k = 0) \approx \frac{1}{2} \frac{\epsilon_0}{c} \left(\frac{\omega_1 \chi^{(2)}}{2n(\omega_1)} \right)^2 I_1^2 \cdot z^2.$$

Figure 1.6 shows the intensity course of the second harmonic along the optical axis for perfect phase matching $\Delta k = 0$ and miss alignment $\Delta k > 0$.

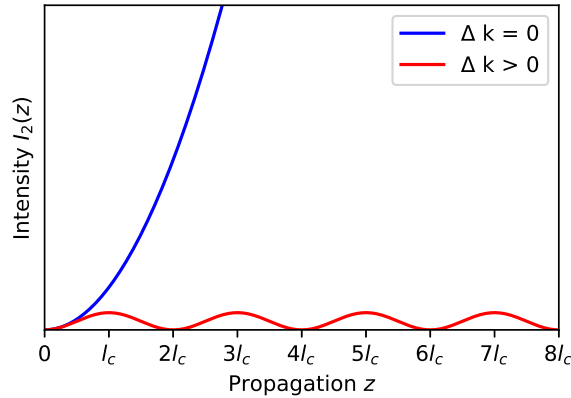


Figure 1.6: Intensity course of the second harmonic along the optical axis for perfect phase matching $\Delta k = 0$ and a phase match missalignment $\Delta k > 1$.

1.2.3 Birefringent phase matching

As was derived in the previous section, the phase matching condition is:

$$n(\omega_1) = n(\omega_2) \quad (1.46)$$

and therefore $n(\omega_1) = n(2\omega_1)$ for the refractive index n of the material. This cannot be realised due to the chromatic behaviour of the material. As shown in 1.7, the phase matching condition can only be achieved by having two refractive indexes for two different beams. This behaviour is called birefringence and is caused by the crystal structure.

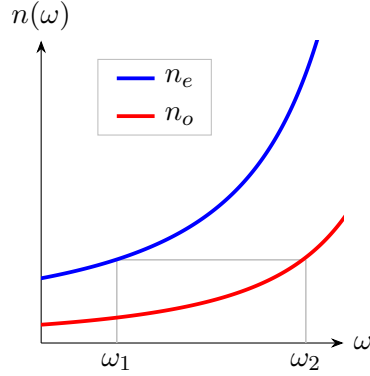


Figure 1.7: Area of normal dispersion in a birefringent material viewing the refractive index for ordinary o and extraordinary e beam polarisation.

A uniaxial material has different refractive indexes regarding its own basis a , b and c :

$$n_a(\omega) \neq n_b(\omega) \neq n_c(\omega).$$

For biaxial materials:

$$n_a(\omega) = n_b(\omega) \neq n_c(\omega).$$

Aligning the basis of an uniaxial material along the optical basis in a way that $b = y$ and a , c are tilted by the angle θ regarding x and z .

Considering the ordinary beam being polarised along the y -axis and the extraordinary along the x -axis and both propagating along the optical axis z , the polarisation in the basis of the crystal remains the same for y -polarisation but the x -polarisation is rotated for the angle θ regarding the axis a . Therefore the refractive index for the extraordinary beam $n_e(\omega, \theta)$ is

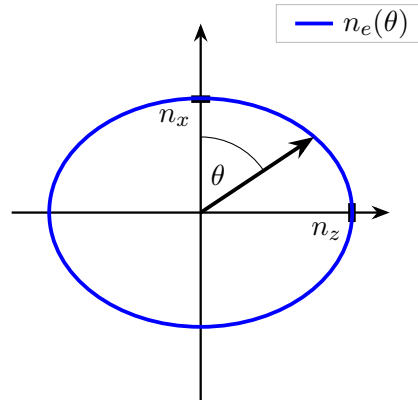


Figure 1.8: Dependency of the refractive index n_e for the extraordinary beam with tilting angle θ of the crystal axes in respect to the optical basis and the refractive indexes n_a and n_c in the basis of the crystal.

dependent on the tilting angle θ of the crystal as depicted in figure 1.9 while the refractive index for the ordinary beam remains constant.

The refractive index for the extraordinary beam can be derived from the classical ellipsis relation:

$$\frac{x^2}{n_x^2} + \frac{z^2}{n_z^2} = 1,$$

using the relations of the polar transformation:

$$\begin{aligned} x &= n \cdot \cos(\theta), \\ z &= n \cdot \sin(\theta), \end{aligned}$$

where the resulting refractive index is dependent on the refractive indexes in the rotational plane and the rotation angle θ also known as the radius of an ellipse:

$$n_{x,z}(\theta) = \frac{n_x \cdot n_z}{\sqrt{(n_x \cdot \sin(\theta))^2 + (n_z \cdot \cos(\theta))^2}}. \quad (1.47)$$

To fulfill the phase matching condition (1.46), the refractive index of ordinary and extraordinary beam must be equal. By plotting the refractive indexes for the two beams in polar coordinates dependent on the tilting angle θ yields a circular graph for the ordinary and an elliptical for the extraordinary beam as depicted in figure 1.9 on the left side. It shows four cross sections of the refractive indexes which can be used for phase matching.

For a biaxial material, the graph would only show two intersections as shown in 1.9 on the right.

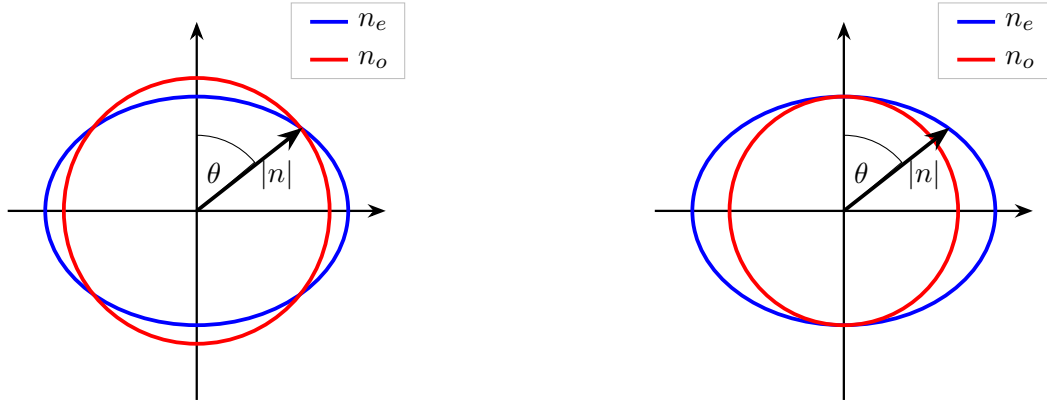


Figure 1.9: Refractive indexes of ordinary and extraordinary beam regarding the tilting angle θ in polar coordinates of a uniaxial material with $n_x < n_y < n_z$ (left) and a biaxial material with $n_x = n_y < n_z$ (right) where the ordinary beam is aligned on the y -axis and the extraordinary beam in the xz -plane.

Therefore orientation of the crystal regarding the optical axis is crucial for phase matching.

1.2.4 Quasi phase matching

For full phase matching a material with refractive indexes n_a and n_b is needed, where $\Delta n = n_a - n_b$ is big enough to ensure both frequencies can experience the same refractive index

as shown in figure 1.7. Where full phase matching is impossible or costly, a more handy alternative is quasi phase matching. Quasi phase matching is accomplished with a periodically poled material which is shown in figure 1.10.

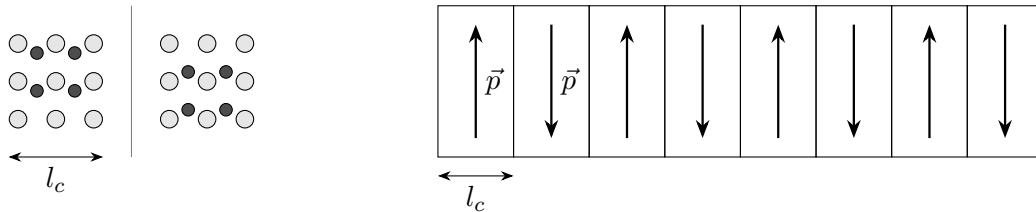


Figure 1.10: Lattice and schematic of a periodically poled material with coherence length l_c .

A material which is doped usually shows dipolic character inside caused by the atomic structure and differently charged atoms. These dipoles can be periodically aligned by applying high voltage to the material in a periodic manner.

Considering a beam propagating through unpoled material, the intensity oscillates along the optical axis for a mismatch in phase $\Delta k \neq 0$. The periodically poled material however changes the sign of the susceptibility and therefore the course of the intensity after every periodicity. Polarising the material periodically according to the coherence length l_c as described by (1.45), the generated photons gain an additional phase shift of 180° per multiple of the coherence length. Instead of interfering destructively, the photons interfere constructively and hence the intensity is constantly increasing as depicted in 1.11 alongside the conventional phase matching cases. The periodically poled structure results in a periodic susceptibility of

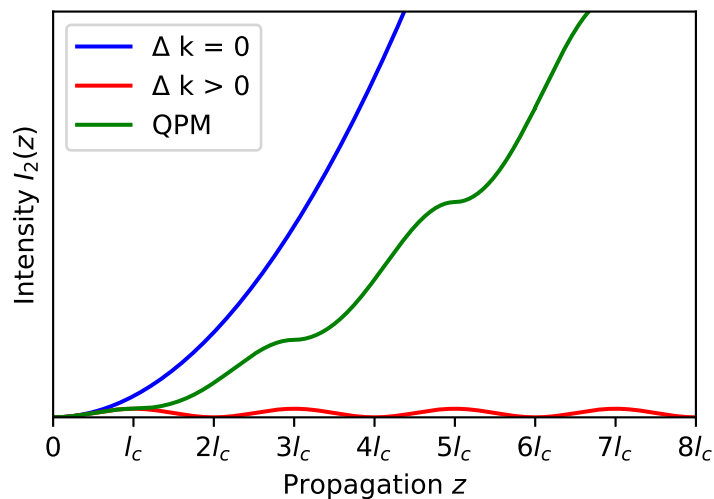


Figure 1.11: Intensity course of the second harmonic along the optical axis for perfect phase matching $\Delta k = 0$, phase match miss alignment $\Delta k > 0$ and quasi phase matching (QPM).

the material. Considering a crystal with n sections, the susceptibility becomes:

$$\chi_n = \chi_0^{(2)}(-1)^n. \quad (1.48)$$

Calculating the amplitude function A_2 for the second harmonic frequency ω_2 as in section 1.2.2 with the additional condition (1.48):

$$A_2 = -\frac{i\omega_1^2 \chi_0^{(2)}}{k_1 c^2} \frac{\chi_0^{(2)}}{2} A_1(z) A_1(z) \sum_{n=0}^{N-1} (-1)^n \int_{l_c n}^{l_c(n+1)} e^{-i\Delta k z} dz,$$

where l_c is the coherence length. Solving the integral yields:

$$A_2 = -\frac{\omega_1^2 \chi_0^{(2)}}{k_1 c^2 \Delta k} \frac{\chi_0^{(2)}}{2} A_1(z) A_1(z) \sum_{n=0}^{N-1} (-1)^n \left(e^{-i\Delta k l_c(n+1)} - e^{-i\Delta k l_c n} \right)$$

Rearranging:

$$A_2 = -\frac{\omega_1^2 \chi_0^{(2)}}{k_1 c^2} \frac{\chi_0^{(2)}}{2} A_1(z) A_1(z) \frac{e^{-i\Delta k l_c} - 1}{\Delta k} \sum_{n=0}^{N-1} (-1)^n e^{-i\Delta k l_c n}.$$

Using the relation of the geometric series with $|q| < 1$:

$$\sum_{k=0}^n a_0 q^k = a_0 \frac{1 - q^{n+1}}{1 - q},$$

the amplitude function can be described by:

$$A_2 = \frac{\omega_1^2 \chi_0^{(2)}}{k_1 c^2} \frac{\chi_0^{(2)}}{2} A_1(z) A_1(z) \frac{1 - e^{-i\Delta k l_c}}{\Delta k} \left(\frac{1 - (-1)^N e^{-i\Delta k l_c N}}{1 + e^{-i\Delta k l_c}} \right).$$

The intensity function can be derived as in section 1.2.2:

$$I_2 = \frac{1}{2} \frac{\epsilon_0}{c} \left(\frac{\omega_1 \chi^{(2)}}{2n(\omega_1)} \right)^2 \cdot I_1^2 \cdot l_c^2 \cdot \frac{\sin^2 \left(\frac{1}{2} \Delta k l_c \right)}{\left(\frac{1}{2} \Delta k l_c \right)^2} \cdot \left(\frac{1 - (-1)^N \cos \left(\frac{1}{2} \Delta k l_c N \right)}{1 + \cos \left(\frac{1}{2} \Delta k l_c \right)} \right)$$

1.3 Stimulated emission

1.3.1 Atom light interaction

Atomic states have fixed energy levels determined by quantum mechanics. Electrons occupy the so called ground state in equilibrium which represents the lowest energy of the system. Electrons can be excited to a higher energy state, for example by excitation with photons. Hereby the energy of the photon must match the energy difference of the states involved in the transition. This condition is expanded for a frequency band due to the natural linewidth of the state itself. An excited electron will decay to a lower energy level in a characteristic time period τ , the lifetime of a state. The absorption and spontaneous emission process of a two state system interacting with a photon is shown in figure 1.12.

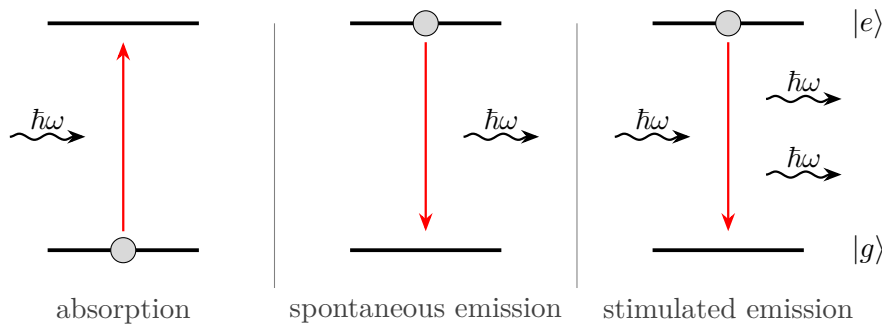


Figure 1.12: Atom light interaction of a transition between ground $|g\rangle$ and excited $|e\rangle$ state of an atom.

A spontaneously emitted photon has the same energy, but random phase, polarisation and propagation direction compared to the excitation photon. Considering a transition between states without dipole fields, the transition state itself has a dipole moment. Applying an external field corresponding to the transition frequency, the probability of the transition increases. This also applies for the decay transition. For stimulated emission, the emitted photon has the same energy, phase, polarisation and propagation direction as the external field represented by photons. A physical system in (thermal) equilibrium occupies its lowest state, the ground state and therefore absorption takes a big role in the interaction process, while the probability of stimulated emission is also decreased by spontaneous emission. The Boltzmann distribution describes the probability of a system to be in a certain state for a given temperature. For infinite temperatures, an evenly distributed population of the states population can be achieved.

By inverting the population in a way that more electrons occupy the higher energy state than the lower one, stimulated emission is more likely than absorption. Population inversion can be achieved by applying a high intensity field to a system with three states as depicted in 1.13. The so called pump laser excites the electrons of state $|0\rangle$ to $|2\rangle$ with frequency ω_1 while the probe laser operates on the transition frequency ω_2 between the states $|0\rangle$ and $|1\rangle$.

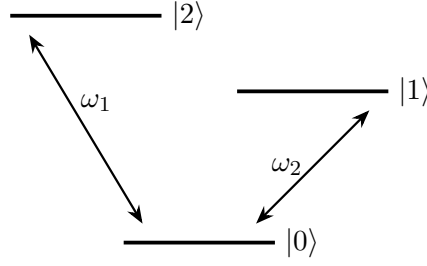


Figure 1.13: A three level system with a ground state $|0\rangle$ and two excited states $|1\rangle$ and $|2\rangle$.

Considering many electrons being excited to state $|2\rangle$ and decaying naturally to state $|1\rangle$ and then either decaying naturally or by stimulated emission to the ground state $|0\rangle$. The lifetime of state $|2\rangle$ needs to be short compared to the lifetime of state $|1\rangle$. This ensures that the excited atoms decay and state $|1\rangle$ is populated quickly. The comparatively long lifetime of state $|1\rangle$ ensures population inversion $N_1 > N_0$, where N_i is the number of occupied atoms in state i . Additionally, the atoms in state $|1\rangle$ are more likely for stimulated emission by the electromagnetic field. The atoms stimulated to emit are than available for repeated excitation by the pump laser.

The same description applies to a gas of many atoms with few or only one electron per atom iterating the described transitions.

1.3.2 Mathematical description

A detailed description for the following calculations can be found in [19].

Considering a gas of three-level atoms as depicted in 1.13, probe and pump laser operating on the transition frequencies from $|0\rangle$ to $|1\rangle$ and $|0\rangle$ to $|2\rangle$ respectively. A high pump power ensures a depopulated ground state $|0\rangle$ and a high populated excited state $|2\rangle$. The rate equation for the excited state $|2\rangle$ is determined by:

$$\frac{d}{dt}N_2 = \gamma_{0,2} (N_0 - N_2) - \frac{N_2}{\tau_{2,0}} - \frac{N_2}{\tau_{2,1}}, \quad (1.49)$$

where $\tau_{i,j}$ is the decay lifetime for a transition from state i to state j , $N_0 - N_2$ is the number of atoms available in the ground state for pumping and $\gamma_{0,2}$ is the probability of an atom making the transition. The transition probability is given by:

$$\gamma_{i,j} = B_{i,j}\rho(\nu),$$

with the Einstein coefficient B for absorption and stimulated emission and $\rho(\nu)$ the radiation density of field. The rate equation for excited state $|1\rangle$ is given by:

$$\frac{d}{dt}N_1 = \frac{N_2}{\tau_{2,1}} - \frac{N_1}{\tau_{1,0}}. \quad (1.50)$$

It is solely given by the atoms decaying to state $|1\rangle$ from $|2\rangle$ and those decaying from $|1\rangle$ to the ground state $|0\rangle$. For a stable population inversion $N_1 > N_0$, the steady state condition

$$\frac{d}{dt}N_2 = \frac{d}{dt}N_1 = 0, \quad (1.51)$$

has to be fulfilled. Using the rate equation (1.49) of state $|2\rangle$, relation (1.51) and considering the decay transition from $|2\rangle$ to $|0\rangle$ as neglectable:

$$\gamma_{0,2}(N_0 - N_2) - \frac{N_2}{\tau_{2,1}} = 0 \quad (1.52)$$

$$\gamma_{0,2}N_0 = N_2 \left(\frac{1}{\tau_{2,1}} + \gamma_{0,2} \right). \quad (1.53)$$

For a stable population inversion, the lifetime $\tau_{2,1}$ should be comparebly small to $\tau_{1,0}$:

$$\tau_{2,1} \ll \tau_{1,0}.$$

This results in:

$$\frac{1}{\tau_{2,1}} \gg \gamma_{0,2}.$$

The population relation between the excited state $|2\rangle$ and the ground state $|0\rangle$ can therefore be described by:

$$\gamma_{0,2}\tau_{2,1}N_0 = N_2.$$

The population on the excited state $|2\rangle$ depends on the pump rate, lifetime of the state $|2\rangle$ and the population of the ground state $|0\rangle$. The same calculation for the excited state $|1\rangle$ yields:

$$N_1 = N_2 \frac{\tau_{1,0}}{\tau_{2,1}}.$$

For considerable stimulated emission, the population difference:

$$\Delta N = N_1 - N_0 = N_2 \left(\frac{\tau_{1,0}}{\tau_{2,1}} - \frac{1}{\gamma_{0,2}\tau_{2,1}} \right),$$

needs to be $\Delta N \geq 0$.

2 Setup

2.1 Optical setup

Figures 2.1 and 2.2 show a schematic of the optical setup used in this thesis.

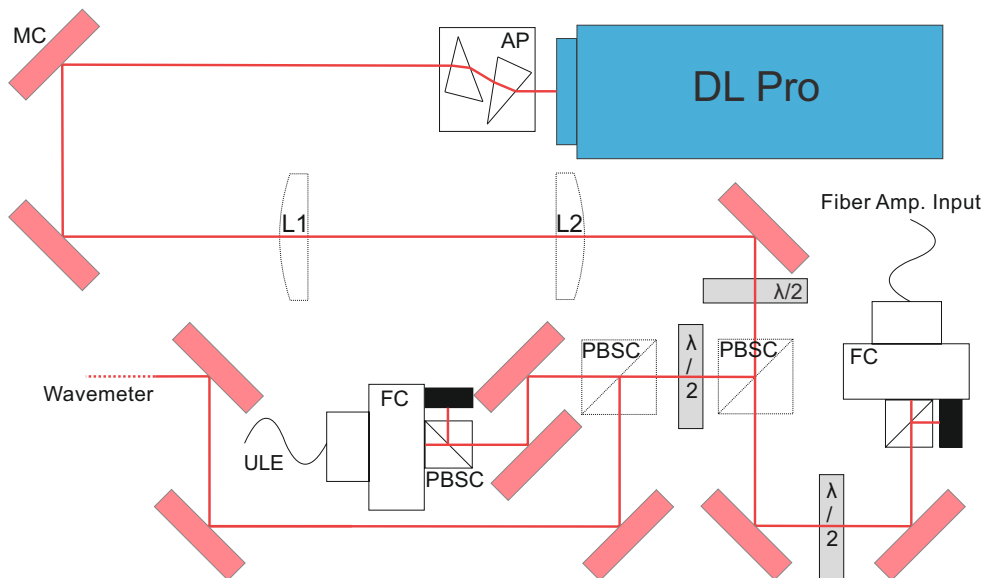


Figure 2.1: Schematic of the experimental setup of the first part with the optical components described below.

Specifications of the optical components used in the setup:

$\frac{\lambda}{2}$ Zero order waveplates for 1080nm

MC C-coated High reflective (HR) mirror for 750-1100 nm

L1 Lens with $f = 100\text{mm}$

L2 Lens with $f = 100\text{mm}$

FC Fiber coupler with $f = 7,5\text{mm}$ length and singlemode fiber.

AP Anamorphic prism pair

PBSC Polarising beam splitter cube

DLPro laser (see 2.2)

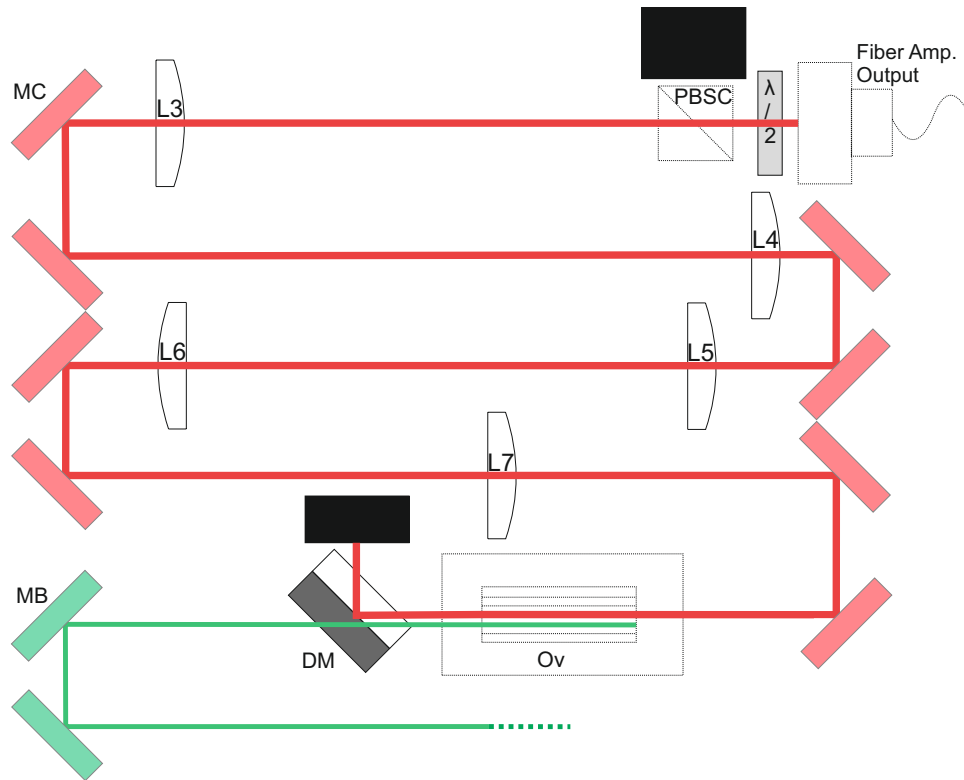


Figure 2.2: Schematic of the experimental setup with the optical components described below.

Specifications of the optical components used in the setup:

$\frac{\lambda}{2}$ Zero order waveplates for 1080 nm

MC C-coated mirror (HR 750-1100 nm)

MB B-coated mirror (HR 400-750 nm)

L3 Lens with $f = 500$ mm

L4 Lens with $f = 100$ mm

L5 Lens with $f = 300$ mm

L6 Lens with $f = 100$ mm

L7 Lens with $f = 200$ mm

DM Dichroic mirror ($R < xy$ nm, $T > xy$ nm)

PBSC Polarising beam splitter cube

Ov Oven with PPLN crystal

2.1.1 Beam path of the setup

The following steps are carried out to achieve an easily recognizable beam path on the optical table. The beam path was chosen to propagate along a grid of holes on the table for attaching optical elements. Furthermore the beam propagates at a height of 10 cm above the table. For inserting lenses, the beam is first aligned without the lens and the lens is inserted in a way that the path behind it doesn't deviate from the original beam path.

Part I: Low power beam at 1080 nm

Beginning at the DL Pro laser with specifications described in 2.2, the beam of wavelength 1080 nm is directed through an anomorphic prism pair. The first prism refracts the light in a way that the elliptical shaped beam is projected on the second prism as circularly shaped beam. By adjusting the angles of the prisms with respect to each other, the size of the beam can be shaped in the plane of the beam. In this case, the beam of size $\omega_x = 0.641$ mm and $\omega_y = 1.202$ mm was shaped into a beam of size $\omega_x = 0.606$ mm and $\omega_y = 0.617$ with lens 1 and lens 2 collimating the beam. The used lenses have both a focal length of $f = 100$ mm and are positioned at a distance of $d \neq f_1 + f_2$. The slight miss alignment of the lenses is used to collimate the beam. A Gaussian beam can never be truly collimated, in further discussions „collimate“ is used to describe a beam which diverges in a neglectable magnitude with respect to the following optical propagation. The collimated beam is then directed through $\frac{\lambda}{2}$ -Waveplates, divided by Polarising Beam Splitter Cubes (PBSC - depicted in 2.3) and then coupled into fibers. A $\frac{\lambda}{2}$ -Waveplate is made of a birefringent material, which

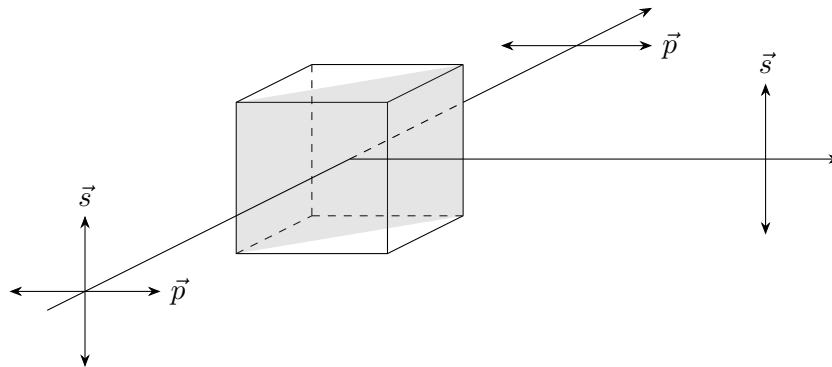


Figure 2.3: Schematic of the working principle of a Polarising Beam Splitter Cube (PBSC).

causes the projected electric field of the beam to have different velocities with respect to the waveplate's axes. The length of the waveplate is hereby chosen to cause a $\frac{\lambda}{2}$ -shift in phase and therefore a rotation of the polarisation dependent on the polarisation of the beam in front of the waveplate and the orientation of the waveplate. This way the intensity split by the PBSC regarding their polarisation (horizontal and vertical) can be adjusted by rotating the waveplate. The vertical polarised component is then reflected from the PBSC while the horizontal component is transmitted. The couplers used in this setup are self built as depicted in figure 2.4, consisting of a lens to focus the beam into the fiber and a rotatable PBSC to adjust the angle of polarisation of the transmitted beam. This is required that the polarisation of the beam corresponds to the polarisation maintained by the fiber. A $\frac{\lambda}{2}$ -Waveplate in front

of the cube rotates the polarisation of the beam to adjust the ratio of transmission through the cube.

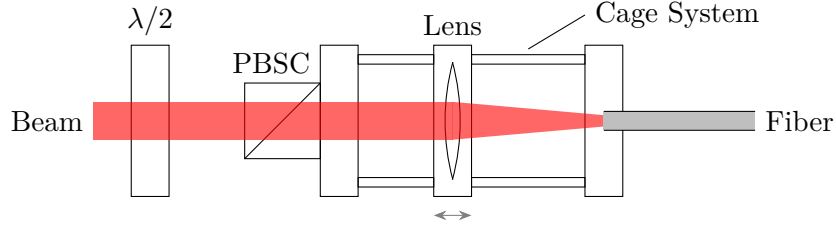


Figure 2.4: Schematic of a fiber coupler for a polarisation maintaining single mode fiber with PBSC, focusing lens and fiber mounted on a cage system.

Equation (2.1) from [20] can be used to calculate the focal length of the coupling lens.

$$f = \frac{\pi D \cdot \text{MFD}}{4\lambda}. \quad (2.1)$$

The Mode Field Diameter (MFD) describes the transverse extent of the optical intensity distribution of a mode, D is the beam diameter at the position of the coupling lens and λ the wavelength. Two mirrors in front of the coupler are used to alter the vertical and horizontal angle as well as the position of the beam regarding the coupling lens. There are two fibers guiding the laser in this part of the setup: one goes to the setup of the ultra low expansion (ULE) cavity and the second one to the fiber amplifier. A polarisation maintaining singlemode fiber is used for both couplers to obtain the gaussian mode and a well defined polarisation. The fiber amplifier amplifies the input signal depending on the set amplification current of the device. The outgoing fiber goes to the second part of the setup. A free running beam leaves this part of the setup to be coupled into a multimode fiber and then directed to a wavemeter to observe the wavelength of the DL Pro laser.

Part II: High power beam at 1080 nm

The beam is coupled out using a collimator and has the shape $\omega_x = 2.256$ mm, $\omega_y = 2.203$ mm. For efficient second harmonic generation, the spatial intensity of the beam inside the crystal needs to be maximized. This is generally achieved by focusing the beam onto a small spot.

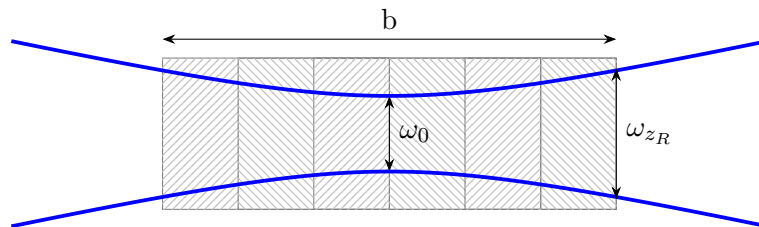


Figure 2.5: Focusing a gaussian beam onto the Periodically Poled Lithium Niobate crystal.

For this setup the beam characteristics at the position of the PPLN crystal are set to be $\omega_0 < 0.353$ mm, $z_R > 20$ mm and therefore $b > 40$ mm as depicted in figure 2.5. This results

in a beam waist of $\omega_{z_R} < 0.5$ mm which needs to be smaller than the width $\Delta = 0.5$ mm of the input facet of the periodically poled region. This is achieved by a lens system of five lenses. Lens 3 and 4 act as a telescope to reshape the beam with a ratio of 5:1 to the waist size of $\omega \approx 0.44$ mm. An optical telescope can be used to alter the size of the beam as depicted in figure 2.6. A Fresnel Rhomb is used to alter the polarisation of the beam for phase matching.

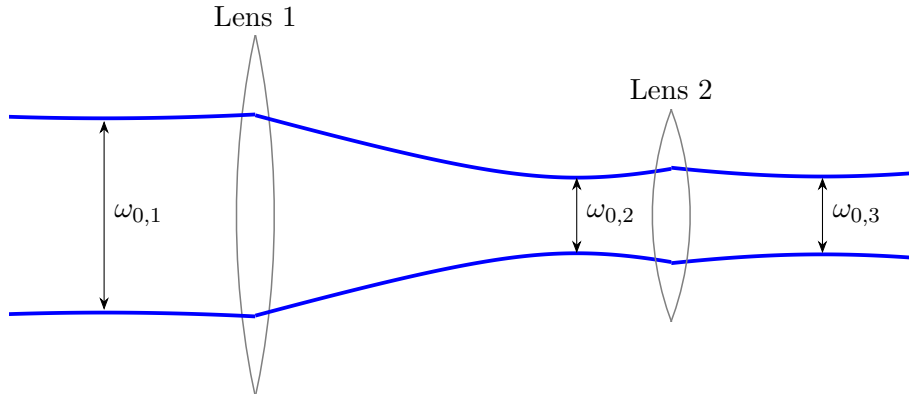


Figure 2.6: Schematic of the beam shaping telescope with the focal lengths $f_1 \gg f_2$.

Lens 5 and 6 also act as a telescope with the focusing ratio of 3:1 to achieve a beam size of $\omega \approx 0.147$ mm. Lens 7 focuses the beam onto the crystal and only changes the position of the focal point and the Rayleigh length z_R . The positions of the lenses to achieve the needed beam characteristics can be calculated via a programmed code using the wave matrix formalism described in 1.1.5.

Part III: High power beam at 540 nm

The beam behind the PPLN crystal contains the second harmonic and a part of the fundamental frequency. The beam is collimated by a lens and directed through a dichroic mirror which reflects the fundamental and transmits the second harmonic. The beam is then directed to the setup for the excitation of nitric oxide from the $A^2\Sigma^+$ state to the $H^2\Sigma^+$ state.

2.2 List of devices

2.2.1 Diode laser

A Diode Laser (DL) Pro from Toptica described in the manual from Toptica Photonics [21] is used for generation of a laserbeam of wavelength $\lambda = 1080$ nm. The wavelength can be coarse tuned between 1000 nm and 1085 nm. The measured output power is 170 mW. It is a laser of Littrow configuration. The light is collimated by a lens and then directed to the diffraction grating as shown in 2.7. The zero order light will be refracted to leave the system while the first order will be refracted back being focused by the lens and onto the facet of the semiconductor. This creates an external cavity for a high reflectivity of the facet. This laser setup is also called External Cavity Diode Laser (ECDL). The grating serves as frequency selective element which allows to adjust the wavelength of the laser within a bandwidth. The wavelength can also be adjusted via current and temperature. The result is a tunable laser diode. The Free Spectral Range (FSR) of the outer cavity is smaller than the one of the diode laser cavity and therefore the finesse is higher.

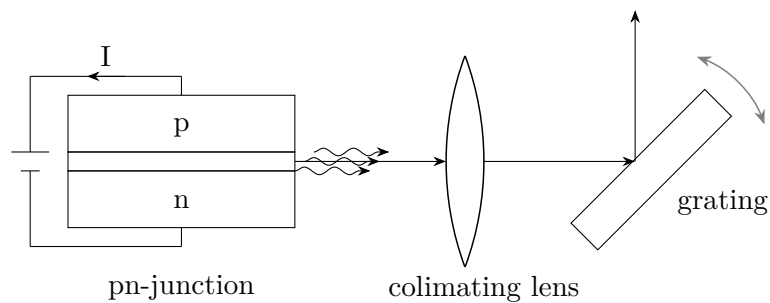


Figure 2.7: Setup scheme of a diode laser with colimating lens and rotatable grating creating an external cavity.

2.2.2 Optical (fiber) amplifier

The specifications of the fiber amplifier are listed in table 2.8. For the wavelength of interest,

Bandwidth of Operation	1060 to 1090 nm
Bandwidth	< 100 kHz
Output Power	up to 40 dBm (10 Watt)
Power Control (APC)	31.7 - 40.5 dBm
APC tunability	15-100%
Booster Current	0.6 - 9.24 Ampere
Preamplifier Current	8 Ampere
Input Power	0-15 dBm (1-32 mW)
Polarisation Extinct Ratio of Fiber	17 dB

Figure 2.8: Specifications of the Optical Fiber Amplifier from Keopsys.

a ytterbium doped silica core with a broad absorption band of 850 – 1070 nm allows a wide selection of pump source while having a broad emission range from around 1060 to 1090 nm. While the pump is being absorbed in the cladding, the seed induces stimulated emission in the core [22, 23].

2.2.3 Periodically Poled Lithium Niobate (PPLN)

A schematic of the PPLN used in this setup is shown in 2.9. It has five poled areas with different periodicity to cover the process of second harmonic generation for fundamental wavelengths from 1068 to 1106 nm.

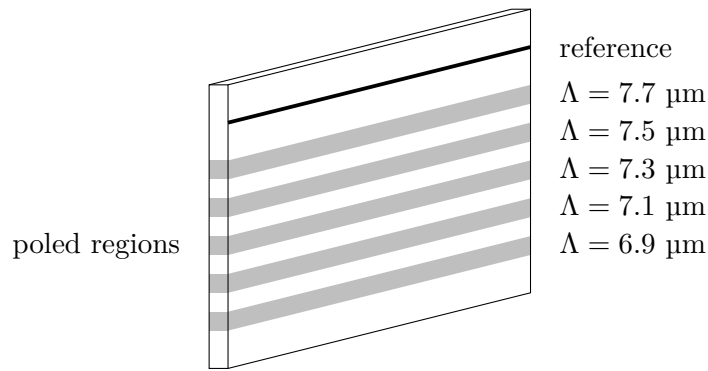


Figure 2.9: Schematic of the periodically poled lithium niobate crystal with different regions of periodicity length Λ provided by the distributor [24].

As in [25] described, quasi phase matching for extraordinary waves is achieved by satisfying:

$$2\pi \left[\frac{n_e(\lambda_1, T)}{\lambda_1} - \frac{n_e(\lambda_2, T)}{\lambda_2} - \frac{n_e(\lambda_3, T)}{\lambda_3} - \frac{1}{\Lambda(T)} \right] = \Delta k_{Opt},$$

where $\Lambda(T)$ is the poling period with thermal expansion taken into account, Δk_{Opt} the optimal phase mismatch. For second harmonic generation the fundamental wave is given by $\lambda_f = \lambda_2 = \lambda_3$ and the second harmonic by $\lambda_1 = \frac{1}{2}\lambda_f$.

The Sellmeier equation yields [25, 26]:

$$n_e^2 = a_1 + b_1 f + \frac{a_2 + b_2 f}{\lambda^2 - (a_3 + b_3 f)^2} + \frac{a_4 + b_4 f}{\lambda^2 - a_5^2} - a_6 \lambda^2,$$

where a_3 , a_5 and a_2 , a_4 account for poles in UV and IR respectively, a_1 the contributions from plasmons in the far UV and a_6 the phonon absorption in the far IR. b_i account for thermal effects, where f from [25] is given by:

$$f = (T - 24.5^\circ C)(T + 570.82).$$

The wavelength dependency on temperature for optimal phase matching is given by a linear function.

3 System Characterisation

3.1 Knife edge measurements

3.1.1 Conventional knife edge measurement

The Gaussian beam parameters ω_0 , z_R and θ_0 (described in chapter 1.1.3) can be determined by measuring the intensity distribution along two axes perpendicular to the optical axis and at different positions z on the optical axis. The power of the laser beam, which is proportional to the intensity, is measured by a powermeter. The device that is used for the following measurements is depicted in figure 3.1. It was built to cut the beam in the x - and y -axis at a fixed z -position on the optical axis. The remaining intensity behind the blade will be measured by the powermeter.

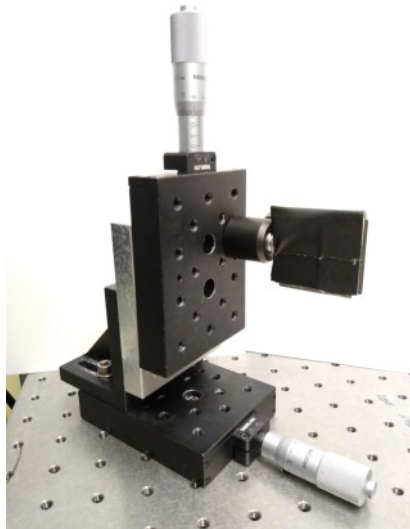


Figure 3.1: A picture of the knife edge device used for the measurements. Razorblades are fixed on the xy -stage.

The edge of the blade will be positioned at the center of the beam and in the middle of the range of the stage to achieve evenly distributed data. This way the measurement includes enough data points of the low intensity parts of the beam on both sides. The blade is then moved away from the beam center at least 3 times the estimated diameter at the position of measurement. For the measurement itself, the blade will be gradually moved through the laserbeam while the corresponding power will be measured.

The intensity profile of the Gaussian beam perpendicular to the optical axis is explained in chapter 1.1.3 and given by (1.28):

$$I(x, y) = I_0 e^{-\frac{2x^2}{\omega_x^2}} e^{-\frac{2y^2}{\omega_y^2}}. \quad (1.28)$$

The total power P_{tot} of the beam is obtained by integrating the intensity distribution. The solution is known from the Gaussian integral [27], I_0 being the maximum intensity:

$$P_{tot} = I_0 \int_{-\infty}^{\infty} dx e^{-\frac{2x^2}{\omega_x^2}} \int_{-\infty}^{\infty} dy e^{-\frac{2y^2}{\omega_y^2}} = \frac{I_0}{2} \pi \omega_x \omega_y. \quad (3.1)$$

The intensity covered by the blade needs to be deducted from the total beam power to obtain the intensity measured at an arbitrary position \tilde{x} of the blade. The integration for y can be carried out as usual with the Gaussian integral:

$$\begin{aligned} P(\tilde{x}) &= P_{tot} - I_0 \int_{-\infty}^{\tilde{x}} dx e^{-\frac{2x^2}{\omega_x^2}} \int_{-\infty}^{\infty} dy e^{-\frac{2y^2}{\omega_y^2}} \\ &= P_{tot} - I_0 \sqrt{\frac{\pi}{2}} \omega_y \int_{-\infty}^{\tilde{x}} dx e^{-\frac{2x^2}{\omega_x^2}}. \end{aligned}$$

The integral over x can be split to obtain one integral which can be solved due to the symmetry of the Gaussian integral:

$$\begin{aligned} P(\tilde{x}) &= P_{tot} - I_0 \sqrt{\frac{\pi}{2}} \omega_y \left[\int_{-\infty}^0 dx e^{-\frac{2x^2}{\omega_x^2}} + \int_0^{\tilde{x}} dx e^{-\frac{2x^2}{\omega_x^2}} \right] \\ &= P_{tot} - I_0 \sqrt{\frac{\pi}{2}} \omega_y \left[\sqrt{\frac{\pi}{2}} \frac{1}{2} \omega_x^2 + \int_0^{\tilde{x}} dx e^{-\frac{2x^2}{\omega_x^2}} \right]. \end{aligned}$$

The latter integral can be represented as the errorfunction by substituting as follows:

$$\begin{aligned} u &= \frac{\sqrt{2}x}{\omega_x} \\ dx &= \frac{\omega_x}{\sqrt{2}} du, \end{aligned}$$

hence:

$$\begin{aligned} P(\tilde{x}) &= P_{tot} - I_0 \sqrt{\pi} \omega_y \left[\frac{\sqrt{\pi}}{2} \omega_x^2 + \omega_x \int_0^{\frac{\sqrt{2}\tilde{x}}{\omega_x}} du e^{-u^2} \right] \\ &= P_{tot} - \frac{P_{tot}}{2} \left[1 + \frac{2}{\sqrt{\pi}} \int_0^{\frac{\sqrt{2}\tilde{x}}{\omega_x}} du e^{-u^2} \right] \\ &= P_{tot} - \frac{P_{tot}}{2} \left[1 + \operatorname{erf} \left(\frac{\sqrt{2}\tilde{x}}{\omega_x} \right) \right]. \end{aligned}$$

The data was fitted with the fit function (3.2) which has the following fit parameters for a proper fit: The deviation x_0 from $x = 0$ caused by the arbitrary stage position, the offset P_0 to compensate the background intensity, the total power P_{tot} and the waist ω_x :

$$P(x) = \frac{P_{tot}}{2} \left[1 \pm \operatorname{erf} \left(\frac{\sqrt{2}(x - x_0)}{\omega_x} \right) \right] + P_0. \quad (3.2)$$

The M^2 parameter defines the quality of a Gaussian beam. While minimal waist ω_0 , wavelength λ and Rayleigh length z_R have a fixed relation as explained in 1.1.4:

$$\omega_0 = \sqrt{\frac{\lambda z_R}{\pi}}, \quad (1.19)$$

the measured Gaussian beam can deviate from this relation. The quality parameter M^2 can be obtained by dividing the real divergence angle by the ideal Gaussian divergence angle:

$$M^2 = \frac{\theta_{\text{real}}}{\theta_{\text{ideal}}} \geq 1. \quad (3.3)$$

The obtained waists ω_x and ω_y of the data sets along the optical z -axis are then fitted with the Gaussian beam width function (1.18) and additional parameters to include an offset z_0 in the direction of the optical axis and the quality parameter M^2 :

$$\omega(z) = \omega_0 \sqrt{1 + (z - z_0)^2 \left(\frac{M^2 \lambda}{\pi \omega_0^2} \right)^2}. \quad (3.4)$$

A python script has been used for the evaluation of the data.

3.1.2 90/10 method

Another and less time consuming way to obtain the beam parameters is the 90/10-method. Hereby the 90 % and 10 % value of the maximum beam intensity is calculated and the positions of the knife along the x - or y -axis of these intensities are located. The distance between both values corresponds to the diameter $D_{90/10}$ of the beam regarding the 90/10 relation. To obtain the common diameter D_{1/e^2} of the beam regarding the $1/e^2$ -relation, the measured values need to be adjusted by (3.5). The $1/e^2$ -diameter describes the width of the beam at an intensity of $\frac{I_0}{e^2}$ where I_0 is the maximum intensity. The power intensity relation 3.1 is used as in the previous section 3.1.1 to evaluate the measured data. Figure 3.2 shows a Gaussian beam with both relations. Using formula (3.2) for determining the relation between $D_{90/10}$ and D_{1/e^2} with the total power set $P_{tot} = 1$:

$$\begin{aligned}
 P(x_{10}) &= 0.1 \cdot P_{tot} = \frac{P_{tot}}{2} \left[1 - \operatorname{erf} \left(\frac{\sqrt{2}x_{10}}{\omega_{1/e^2}} \right) \right] \\
 0.8 &= \operatorname{erf} \left(\frac{\sqrt{2}x_{10}}{\omega_{1/e^2}} \right) \\
 \Rightarrow x_{10} &\approx 0,64 \cdot \omega_{1/e^2}
 \end{aligned}$$

Therefore the measured diameter $D_{90/10}$ can be converted to the D_{1/e^2} -Diameter by:

$$D_{1/e^2} = 1,5625 \cdot D_{90/10}, \quad (3.5)$$

and the waist ω_{1/e^2} by:

$$\omega_{1/e^2} = 0.78125 \cdot D_{90/10}. \quad (3.6)$$

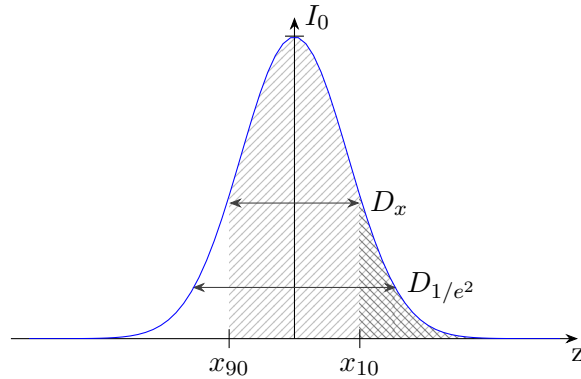


Figure 3.2: Gaussian profile with 90/10 diameter definition $D_{90/10}$ and D_{1/e^2} relation where the integral from x_{10} to ∞ corresponds to 10% of the total intensity.

3.1.3 Chopper method

Figure 3.3 shows a device which has a rotating disc in the xy -plane with a slit of width $b = 6.2$ mm. The disc is rotated by a small motor with constant speed and rotation frequency $f = 0.4$ Hz. The rotating slit will cut the Gaussian beam similarly to the conventional knife edge method. To dissolve the change in power an oscilloscope and a photodiode are used instead of a powermeter. The oscilloscope displays the time dependent signal on the photodiode and calculates the rise time T_ω as well as the signal width T_b . The rise time T_ω is defined as the time between the signal reaches 10 % and 90 % of its maximum value. The simple relation from waist to rise time which equals the width of the slit to the width of the signal ratio is given by:

$$\frac{\omega_{90/10}}{T_\omega} = \frac{b}{T_b}.$$

The $1/e^2$ definition of the waist can be obtained by inserting the relation (3.5):

$$\omega_{1/e^2} = 0.78125 \cdot D_{90/10} = 0.78125 \cdot T_\omega \cdot \frac{b}{T_b}. \quad (3.7)$$

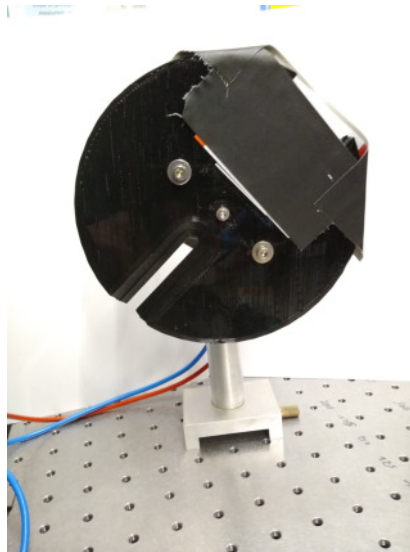


Figure 3.3: A picture of the chopper device used for the measurements.

3.1.4 1080 nm beam at the position of the coupler for the fiber amplifier

For a detailed description of the beam coupled into a single mode polarisation maintaining fiber at the position of the fiber coupler (described in 2.2) leading to the fiber amplifier, a series of knife edge measurements have been carried out. The conventional knife edge measurement for the position $z = 20$ mm with the error fit function (3.2) is shown in figure 3.4 with the fit parameters for all measurements being listed in 3.1 and 3.2. $z_L = 0$ describes the position of the focussing lens of the coupler. The optical components are attached in 25 mm distance to each other, measurements deviating from distances of $n \cdot 25$ mm are more time consuming and therefore not reasonable. The beam at the exact position of the lens can be obtained with the waist function fitted to a series of measurements as shown in figure 3.5 with the error area obtained by using the fit function with the error values of the fit.

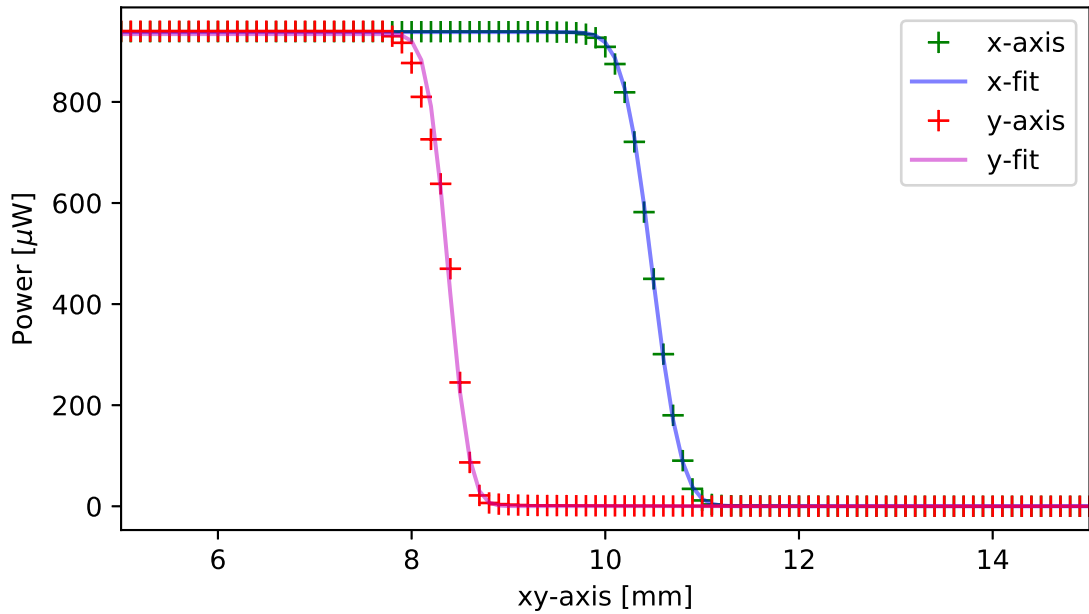


Figure 3.4: Conventional knife edge measurement of the beam at the position of the coupler for the fiber amplifier fitted with the error function (3.2).

z -position [mm]	P_{tot} [μ W]	d [μ W]	x_0 [mm]	ω_x [mm]
-30	963.4	0.2	10.2	0.4975 ± 0.0007
-5	975.4	0.1	10.0	0.5029 ± 0.0007
20	937.9	0.2	10.5	0.4786 ± 0.0007
45	964.4	1.0	10.8	0.4850 ± 0.0007
1070	922.6	0.5	9.4	0.8257 ± 0.0010
1320	920.1	0.9	9.4	1.0011 ± 0.0011

Table 3.1: Fit parameter of the fit function (3.2) for data sets of the x -axis component. Measured along the optical axis at the position of the input coupler of the fiber amplifier.

z -position [mm]	P_{tot} [μ W]	d [μ W]	y_0 [mm]	ω_y [mm]
-30	954.9	5.0	8.4	0.3584 ± 0.0006
-5	974.8	1.3	11.0	0.3725 ± 0.0006
20	933.9	0.4	8.4	0.3474 ± 0.0006
45	962.1	0.4	9.9	0.3652 ± 0.0006
1070	921.9	1.5	10.9	1.0220 ± 0.0011
1320	910.2	1.5	10.1	1.1780 ± 0.0012

Table 3.2: Fit parameter of the fit function (3.2) of data sets for the y -axis component. Measured along the optical axis at the position of the input coupler of the fiber amplifier.

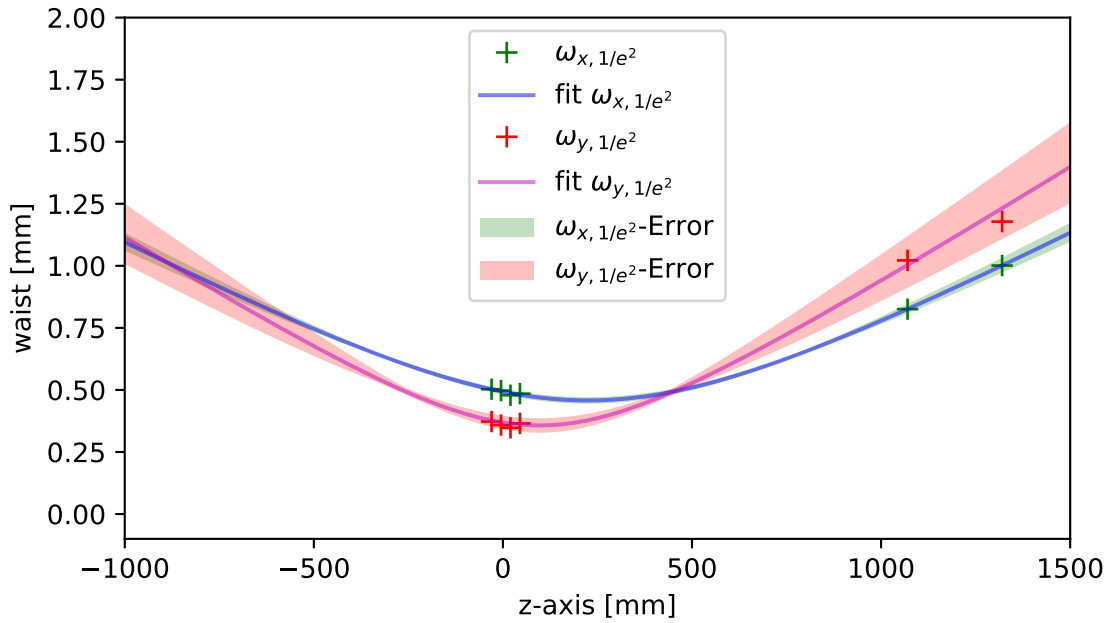


Figure 3.5: Waists obtained from the knife edge measurement for different positions z on the optical axis regarding the position of the lens $z_L = 0$ and the waist function (3.4) fitted.

Axis	Offset z_0 [mm]	Quality factor M	Waist ω_0 [mm]	Rayleigh length z_R [m]
ω_x	224.5 ± 32.8	1.04 ± 0.01	0.4577 ± 0.0134	0.6094
ω_y	-2.0 ± 111.4	1.00 ± 0.02	0.3568 ± 0.0292	0.3703

Table 3.3: Fit parameters of the waist fit function (3.4) for the data sets on x - and y -axis along the optical axis at the position of the coupler for the fiber amplifier and the calculated Rayleigh length z_R from the waist ω_0 with (1.19).

3.1.5 1080 nm beam of the output of the fiber amplifier coupler

Conventional method:

The beam coupled into a single mode polarisation maintaining fiber at an arbitrary position of the setup is leaving the coupler adjusted for the fiber amplifier (input) at an open position on the table. This setup generates the optimal beam for coupling into the fiber and the measurement can be compared to the previous one for coupling into the fiber. Three different measurement techniques were employed for comparison in terms of accuracy and the time needed to perform the measurement. Figure 3.6 shows the conventionally measured beam at the position $z = 5$ mm on the optical axis with the fitted error function (3.2). The fit parameters for all measurements are listed in 3.4 and 3.5. A deviation of 0.5 % of the measured power values due to the fluctuation of the powermeter is considered.

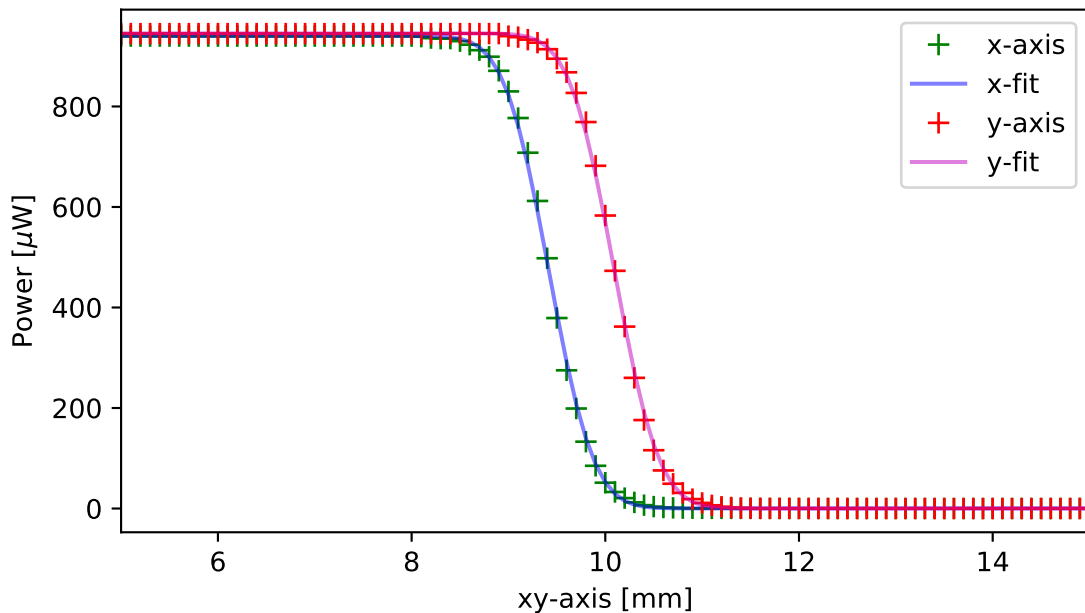


Figure 3.6: Conventional knife edge measurement at the position where the beam is leaving the coupler for the fiber amplifier with the error fit function (3.2).

z -position [mm]	P_{tot} [μ W]	P_0 [μ W]	x_0 [mm]	ω_y [mm]
50	940.1	0.2	9.4	0.7283 ± 0.0009
75	939.4	1.7	9.3	0.7333 ± 0.0009
100	933.4	1.8	9.2	0.7361 ± 0.0009
125	934.5	1.9	9.1	0.7494 ± 0.0010
150	918.8	2.1	8.5	0.7644 ± 0.0010
175	920.6	2.5	8.9	0.7765 ± 0.0010
200	922.2	2.9	8.8	0.7860 ± 0.0010
550	922.2	2.0	8.8	1.1896 ± 0.0012
600	941.7	2.3	8.6	1.2583 ± 0.0013
650	922.2	2.0	8.9	1.2966 ± 0.0013
700	942.9	3.0	8.7	1.3306 ± 0.0013
750	950.1	3.3	9.1	1.4120 ± 0.0013
800	957.3	4.4	9.2	1.4504 ± 0.0013
850	923.7	2.7	9.3	1.4211 ± 0.0014

Table 3.4: Fit parameter of the fit function (3.2) for the data belonging to the x -axis component along the optical axis of the beam leaving the coupler with regard to the position of the lens $z_L = 0$ mm.

z -position [mm]	P_{tot} [μ W]	P_0 [μ W]	y_0 [mm]	ω_y [mm]
50	945.2	0.2	10.1	0.7307 ± 0.0009
75	923.3	0.6	10.0	0.7393 ± 0.0010
100	934.2	0.6	10.1	0.7490 ± 0.0010
125	934.2	0.2	10.0	0.7532 ± 0.0010
150	915.7	0.3	9.9	0.7582 ± 0.0010
175	919.2	0.3	10.0	0.7692 ± 0.0010
200	923.2	0.3	10.1	0.7816 ± 0.0010
550	921.1	0.4	10.2	1.1828 ± 0.0012
600	933.7	0.4	10.2	1.2334 ± 0.0013
650	922.5	0.5	10.4	1.2748 ± 0.0013
700	946.6	0.4	10.4	1.3171 ± 0.0013
750	953.5	0.5	10.2	1.3899 ± 0.0013
800	945.9	0.6	9.8	1.4136 ± 0.0014
850	924.5	0.5	10.3	1.4605 ± 0.0014

Table 3.5: Fit parameter of the fit function (3.2) for the data belonging to the y -axis component along the optical axis of the beam leaving the coupler regarding the position of the lens $z_L = 0$ mm.

Figure 3.7 shows the waists obtained and listed in tables 3.4 and 3.5 fitted with the waist function (3.4). The fit errors for the quality factor M and the beam waist ω_0 and therefore resulting fits within the errors are displayed as coloured areas. The resulting waist parameters from the fit are listed in 3.6.

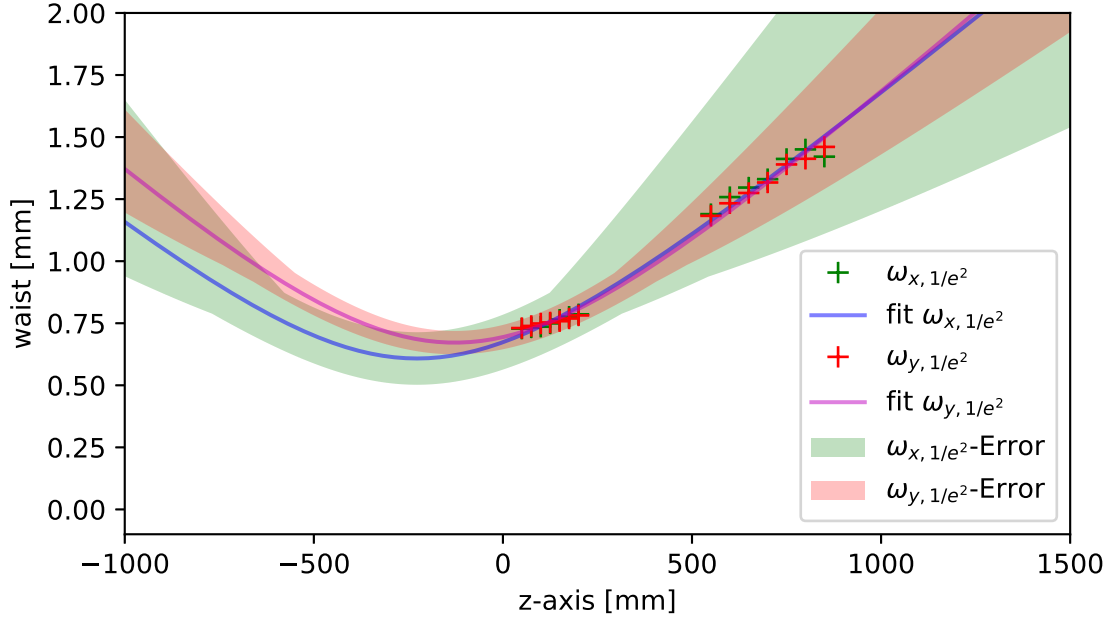


Figure 3.7: Waists obtained from the knife edge measurement for different positions z on the optical axis with regard the position of the lens $z_L = 0$ mm and the waist function (3.4) fitted.

Axis	Offset z_0 [mm]	Quality factor M	Waist ω_0 [mm]	Rayleigh length z_R [m]
ω_x	-227.3 ± 156.1	1.50 ± 0.22	0.6081 ± 0.1059	1.0757
ω_y	-127.5 ± 87.0	1.64 ± 0.12	0.6719 ± 0.0471	1.3132

Table 3.6: Fit parameters of the waist fit function (3.4) for the data sets on x - and y -axis along the optical axis of the beam leaving the coupler regarding the position of the lens $z_L = 0$ mm.

90/10 method:

Additionally, the previously described 90/10 method was used. The measured data and the calculated waists are listed in table 3.7 and 3.8. The waists are calculated with formula (3.5) and an error of 0.5 % for the power values is considered. The relation between the errors and values for power and width are given by:

$$\frac{\Delta P}{\Delta D} = \frac{P_{9010}}{D_{9010}},$$

where ΔP and ΔD are the standard deviation values. P_{9010} and D_{9010} are the measured values.

The waist error can therefore be calculated by:

$$\begin{aligned}\Delta\omega &= 0.78125 \cdot \Delta D = 0.78125 \cdot \frac{\Delta P \cdot x_{9010}}{P_{9010}} \\ &\approx 0.78125 \cdot \frac{(5 \mu\text{W} + 0.5 \mu\text{W}) \cdot 1.92 \text{ mm}}{855 \mu\text{W}} \approx 0.0129 \text{ mm} \\ &= 0.0096 \text{ mm},\end{aligned}$$

with the maximum value measured for $D_{9010} = 1.92 \text{ mm}$ and a averaged power maximum of $950 \mu\text{W}$. Figure 3.8 shows the measured waists on the optical axis with corresponding fits and error areas. The fit parameters obtained by the fit are listed in table 3.9.

z [mm]	P_{tot} [μW]	x_{90} [mm]	x_{10} [mm]	Δx [mm]	$\omega_{1/e,x}$ [mm]
100	932	8.46	9.46	1.00	0.7813
150	932	8.28	9.33	1.05	0.8203
200	932	8.11	9.22	1.11	0.8672
525	942	8.06	9.62	1.54	1.2031
550	9.85	7.82	9.38	1.56	1.2188
575	938	8.07	9.69	1.62	1.2656
600	985	7.88	9.49	1.61	1.2578
625	945	8.23	9.85	1.62	1.2656
650	990	7.91	9.60	1.67	1.3047
675	953	8.27	9.95	1.68	1.3125
700	980	7.98	9.74	1.76	1.3750
725	968	8.34	10.09	1.75	1.3672
750	985	8.03	9.80	1.77	1.3828
775	951	8.28	10.10	1.82	1.4219
800	980	8.13	9.99	1.86	1.4531

Table 3.7: Measured positions of the 10 %, 90 % values of the total power of the knife edge method and the corresponding waist calculated with (3.5) of the x -axis.

z [mm]	P_{tot} [W]	y_{90} [mm]	y_{10} [mm]	Δy [mm]	$\omega_{1/e,y}$ [mm]
100	932	9.75	10.75	1.00	0.7813
150	932	9.54	10.61	1.05	0.8203
200	932	9.61	10.72	1.11	0.8672
525	940	10.93	9.39	1.54	1.2031
550	985	9.27	10.83	1.56	1.2188
575	941	10.33	8.77	1.56	1.2188
600	990	9.24	10.85	1.59	1.2422
625	945	10.34	8.73	1.61	1.2578
650	990	9.41	11.07	1.66	1.2969
675	932	10.18	8.54	1.64	1.2813
700	985	9.37	11.12	1.75	1.3672
725	956	10.54	8.78	1.76	1.3750
750	985	9.23	11.00	1.77	1.3828
775	955	10.63	8.81	1.92	1.5000
800	980	8.13	9.99	1.86	1.4531

Table 3.8: Measured positions of the 10 %, 90 % values of the total power of the knife edge method and the corresponding waist calculated with (3.5) of the y -axis.

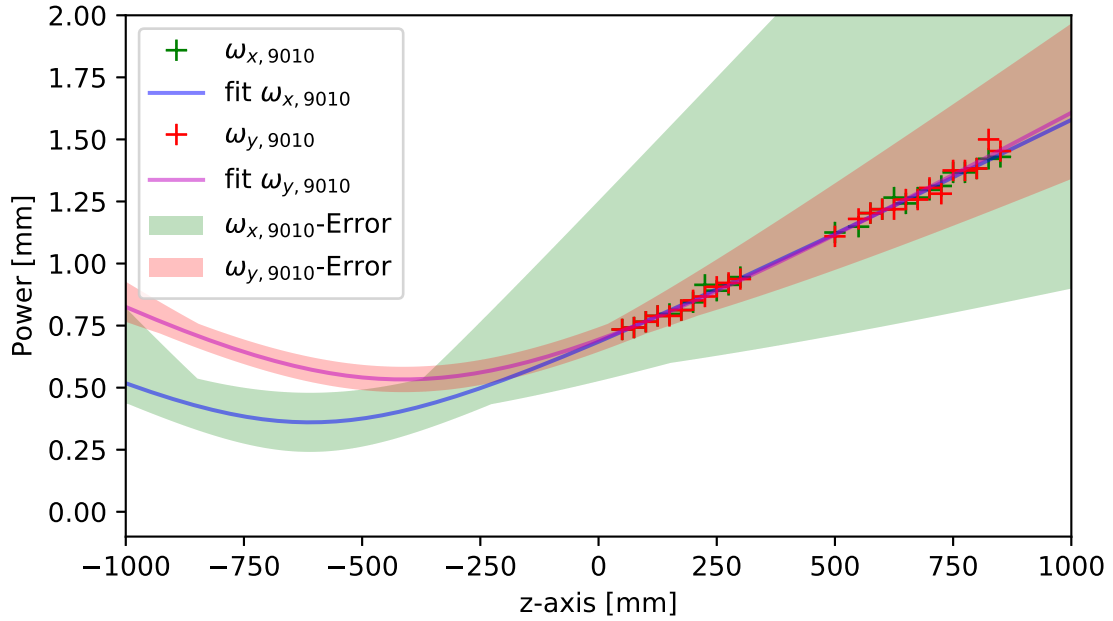


Figure 3.8: Measured waists with the 90/10 Method of the output beam of the coupler on the optical axis with equation (1.18).

Axis	Offset z_0 [mm]	Quality factor M	Waist ω_0 [mm]	Rayleigh length z_R [m]
ω_x	-608.0 ± 49.5	1.00 ± 0.09	0.3595 ± 0.0594	0.3759
ω_y	-453.2 ± 35.1	1.23 ± 0.05	0.5005 ± 0.0299	0.7287

Table 3.9: Fit parameters of the waist fit function (3.4) for the 90/10 measurement on x - and y -axis along the optical axis of the beam leaving the coupler regarding the position of the lens $z_L = 0$ mm.

Chopper method:

Figure 3.9 shows the signal measured with the oscilloscope by cutting the beam as described in 3.1.2.

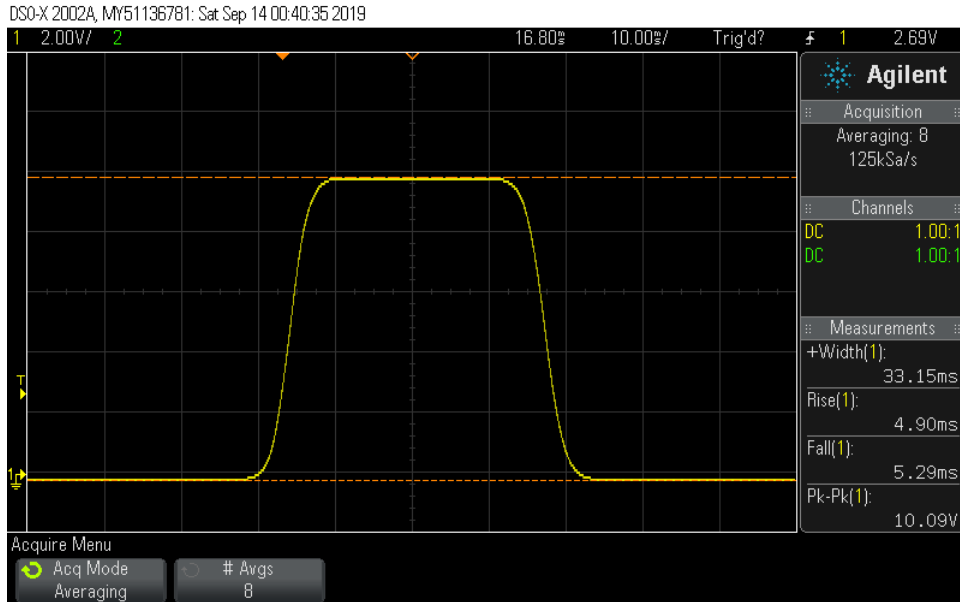


Figure 3.9: Time dependent signal at the oscilloscope of the beam being cut by the chopper with the rise time and peak width measured by the device.

The oscilloscope calculates the rise time T_ω with the 90/10 relation and the peak width T_b . The following errors are considered:

$$\begin{aligned}\Delta T_\omega &= 0.27 \text{ ms}, \\ \Delta b &= 0.05 \text{ mm}, \\ \Delta T_b &= 0.55 \text{ ms}.\end{aligned}$$

The errors for T_ω and T_b are the standard deviation from the median value of the measured data. Δb is the considered measurement error. ΔT_b describes the standard deviation from the medium value, T_ω the standard deviation of the medium value obtained from the rise and fall time. Δb results from the measurement accuracy. The error of the waists can be calculated

by:

$$\begin{aligned}
 \Delta\omega_{1/e} &= \left| \partial_{T_\omega} \omega_{1/e} \right| \cdot \Delta T_\omega + \left| \partial_b \omega_{1/e} \right| \cdot \Delta b + \left| \partial_{T_b} \omega_{1/e} \right| \cdot \Delta T_b \\
 &= \left| \frac{b}{T_b} \cdot 0.78125 \right| \cdot \Delta T_\omega + \left| \frac{T_\omega}{T_b} \cdot 0.78125 \right| \cdot \Delta b + \left| -\frac{T_\omega \cdot b}{T_b^2} \cdot 0.78125 \right| \cdot \Delta T_b \\
 &= \left| \frac{6.2 \text{ mm}}{33.58 \text{ ms}} \cdot 0.78125 \right| \cdot 0.27 \text{ ms} + \left| \frac{8.105 \text{ ms}}{33.58 \text{ ms}} \cdot 0.78125 \right| \cdot 0.05 \text{ mm} \\
 &\quad + \left| -\frac{8.105 \text{ ms} \cdot 6.2 \text{ mm}}{(33.58 \text{ ms})^2} \cdot 0.78125 \right| \cdot 0.55 \text{ ms} \\
 &= 0.0675 \text{ mm}
 \end{aligned}$$

The measured values as well as the calculated waists with (3.7) are listed in table 3.10. The fitted waist function (3.4) is shown in figure 3.10 with the range of the error values represented by a coloured area. The corresponding fit values are listed in 3.10.

z [mm]	$T_{\omega,1}$ [ms]	$T_{\omega,2}$ [ms]	T_b [ms]	$\omega_{1/e}$ [mm]
25	4.99	5.39	33.42	0.7522
50	5.22	5.65	33.65	0.7823
75	5.07	5.68	33.30	0.7717
100	5.47	5.74	33.71	0.8054
125	5.47	5.68	33.76	0.7999
150	5.62	6.10	33.14	0.8565
500	7.52	7.86	32.93	1.1311
525	8.30	8.38	33.17	1.2041
550	7.97	8.24	33.07	1.1691
575	8.35	8.62	32.86	1.2279
600	8.18	8.59	33.23	1.2222
625	8.53	8.83	32.82	1.2913
650	8.74	8.94	32.86	1.3031
675	8.80	9.12	32.56	1.3224
700	8.88	9.28	33.74	1.3035
725	9.17	9.46	33.47	1.3731
750	9.63	9.73	33.58	1.4178
775	9.57	10.16	33.55	1.4406
800	9.46	10.19	33.82	1.4072

Table 3.10: Measured rise time $T_{\omega,1}$, fall time $T_{\omega,2}$ and peak width T_b with the oscilloscope by cutting the beam and the corresponding waist calculated with (3.7).

Axis	Offset z_0 [mm]	Quality factor M	Waist ω_0 [mm]	Rayleigh length z_R [m]
ω	-309.1 ± 157.3	1.42 ± 0.19	0.6141 ± 0.1018	1.0970

Table 3.11: Fit parameters of the waist fit function (3.4) for the chopper measurement along the optical axis of the beam leaving the coupler with regard to the position of the lens $z_L = 0$ mm.

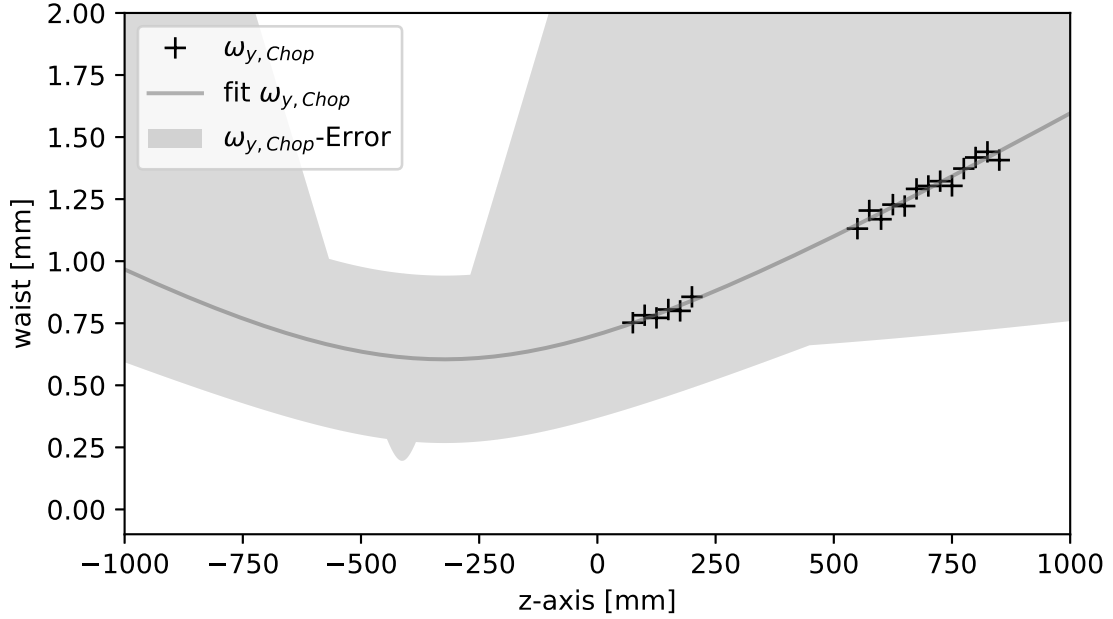


Figure 3.10: Measured waists with the Chopper Method of the output beam of the coupler on the optical axis with the fit function (1.18).

3.1.6 Comparison between the knife edge methods

The measured beam is not optimal for a quantitative beam reconstruction due to the monotonous behaviour of the diverging beam. It allows a reconstruction of the beam within the area of measurement which is sufficient to calculate the coupling efficiency. The input beam has its focus behind the coupler. Therefore the coupling efficiency can not be calculated from the obtained beam data. The fit parameters of the different methods are listed in table 3.12 for comparison. The measured and calculated waists of the methods for the x -axis are plotted in figure 3.11 and the waists for the y -axis in figure 3.11 including the chopper measurement with the error of the fits represented by a coloured area .

Method	Waist	z_0 [mm]	M	ω_0 [mm]	z_R [m]
Conventional	ω_x	-227.3 ± 156.1	1.50 ± 0.22	0.6081 ± 0.1059	1.0757
	ω_y	-127.5 ± 87.0	1.64 ± 0.12	0.6719 ± 0.0471	1.3132
90/10	ω_x	-608.0 ± 49.5	1.00 ± 0.09	0.3595 ± 0.0594	0.3759
	ω_y	-453.2 ± 35.1	1.23 ± 0.05	0.5005 ± 0.0299	0.7287
Chopper	ω	-309.1 ± 157.3	1.42 ± 0.19	0.6141 ± 0.1018	1.0970

Table 3.12: Fit parameters of the knife edge measurement methods of the fit function (3.4) for the obtained data along the optical axis of the beam leaving the coupler regarding the position of the lens $z_L = 0$ mm.

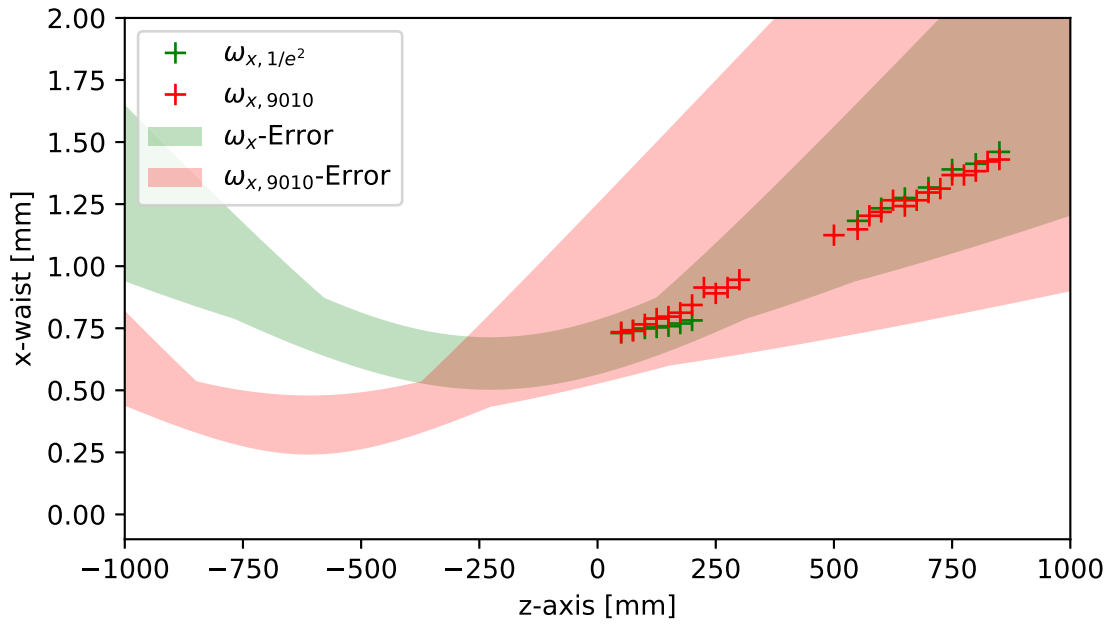


Figure 3.11: Comparison of the different knife edge measurement methods from the obtained data fitted with the fit function (1.18).

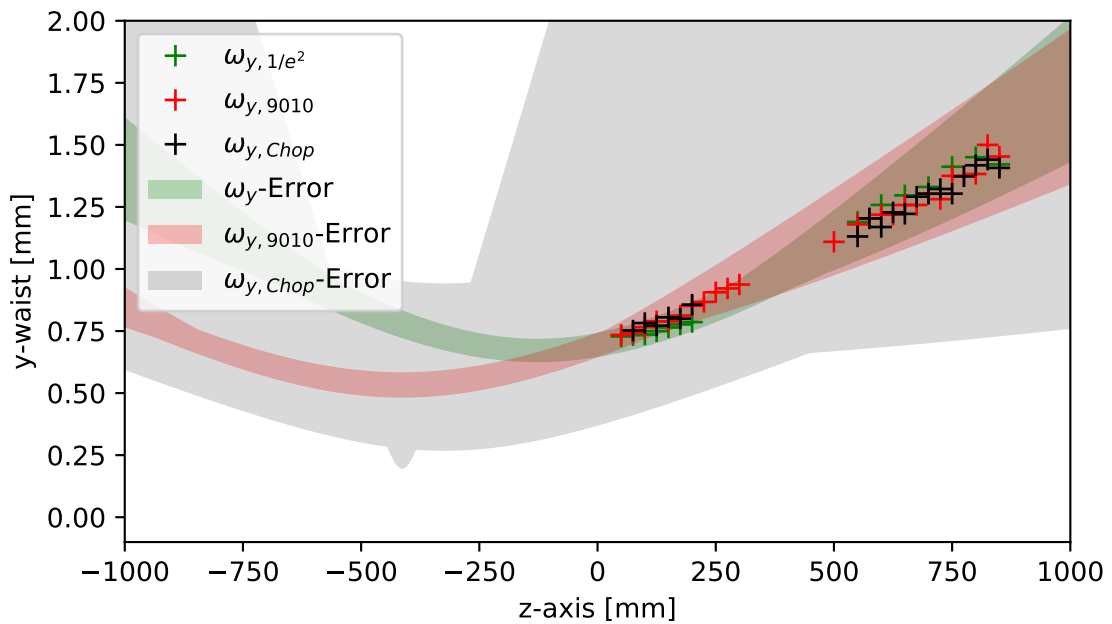


Figure 3.12: Comparison of the different knife edge measurement methods from the obtained data fitted with the fit function (1.18).

Comparing figure 3.5 with figure 3.7, it becomes clear that the fit and the resulting errors are far more precise for a measurement including the waist of the beam. Considering the time needed to take a set of data (ω_x and ω_y at one z -position ≈ 20 minutes)

with the conventional knife edge measurement, the less accurate 90/10 or chopper methods are good enough for most measurements needed within the lab.

The chopper used for the measurements has a standard electro motor and a disc printed with a 3d printer. The dimensions used for calculation are therefore inaccurate compared to the micrometer stages and razor blade of the conventional knife edge method. However, the measurement is less sensitive to power fluctuations which was the main reason to employ this technique while building up the described laser system.

4 Summary and Outlook

4.1 Summary

English

This thesis aimed at the setup and characterisation of a frequency doubled laser system. A diode laser is used as seedlaser with the wavelength $\lambda = 1080$ nm. The Seed laser is then amplified by a fiber amplifier and shaped for passing a Periodically Poled Lithium Niobate (PPLN) crystal. Second harmonic generation takes place in the crystal generating a beam of wavelength $\lambda = 540$ nm.

The setup couldn't be completed due to a defect on the fiber amplifier. Hence, the setup could not be characterised.

The beam leaving the diode laser was collimated with two lenses, split and redirected to three fiber couplers. $\frac{\lambda}{2}$ -Waveplates and Polarising Beam Splitter Cubes (PBSC) are used to control the intensity at each coupler. The Gaussian beam regarding the input and output of a self-built coupler leading to the fiber amplifier was measured with the conventional knife edge method. A comparison of the focused input beam and the diverging output beam is unreasonable. A series of measurements with three different methods, namely the conventional, 90/10 and chopper methods, was conducted on the output beam. Comparing the three methods regarding their errors, the conventional method is the most accurate but also most time consuming method. The downside of the 90/10 method is, that only two datapoints are obtained for the waist at a certain position. This leads to a large sensitivity to fluctuations due to a lack of statistics. The Chopper method is the least time consuming method. The error for the fit is by far larger than for the other measurements. This is caused by the consideration of all measured values, as the slit width b , the peak width T_b and the rise time T_ω . Additionally, due to the setup of the Chopper, the measured waist does not exactly match the y -axis but has a small angle between both axes. The reconstruction of the gaussian beam makes only sense, where the focus lies between the measured data. This is the case for the measured input beam. The fitvalues for the waist ω_0 and the position of the focus z_0 of the output beam are not reliable.

Whenever a Gaussian beam has to be characterised, the conventional measurement should be considered for reasonable data. The 90/10- or Chopper method might be used for a first impression of the beam characterisation, especially to obtain a rough estimate for the position of the focus. This ensures a reasonable choice of positions for the conventional knife edge measurement.

German

Im Rahmen dieser Arbeit sollte ein optischer Aufbau zur Frequenzverdopplung realisiert und charakterisiert werden. Ein Diodenlaser mit der Wellenlänge $\lambda = 1080$ nm wird als Seedlaser verwendet, welcher von einem optischen Faserverstärker verstärkt wird. Durch eine Abfolge von Linsen wird der Strahl auf den frequenzverdoppelnden, periodisch polarisierten Lithiumniobatkristall fokussiert. Der Kristall erzeugt die zweite Harmonische des fundamentalen Laserstrahls bei einer Wellenlänge von $\lambda = 540$ nm.

Durch einen Defekt am Faserverstärker konnte der Aufbau nicht vollendet und folglich auch nicht charakterisiert werden.

Der Strahl des Diodenlasers wurde durch zwei Linsen kollimiert, aufgeteilt und zu drei Faserkopplern umgelenkt. $\frac{\lambda}{2}$ -Verzögerungsplatten und polarisationsabhängige Strahlteiler ermöglichen die Anpassung der Intensität in jedem Strahlarm. Der Gauß'sche Strahl bezüglich des Ein- und Ausgangs des Faserkopplers, welcher zum Faserverstärker führt, wurde für einen Vergleich mit der konventionellen Knife-Edge-Methode vermessen. Ein Vergleich der beiden Strahlen ist nicht sinnvoll, da der Eingangsstrahl an der Position des Kopplers konvergiert, während der Ausgangsstrahl divergiert. Eine Serie von Messungen mit drei verschiedenen Methoden, der konventionellen, der 90/10- und der Chopper-Methode, wurde am Ausgangsstrahl des Faserkopplers durchgeführt. Ein Vergleich der drei Methoden ergibt, dass die konventionelle Messung den geringsten Fehler besitzt, allerdings auch die zeitlich aufwendigste Methode ist. Der Nachteil der 90/10-Methode ist, dass bei ihr lediglich zwei Datenpunkte zur Bestimmung der jeweiligen Strahlradien aufgenommen werden. Daraus folgt eine hohe Anfälligkeit für Fluktuationen verursacht durch fehlende Statistik. Die Chopper-Methode benötigt den zeitlich geringsten Aufwand, hat aber auch einen deutlich größeren Fehlerbereich. Dieser wird durch die Betrachtung aller möglichen Fehler der gemessenen Größen wie der Spaltbreite b , der gemessenen Peakbreite T_b und der Steig- und Fallzeit T_ω erzeugt. Zusätzlich lässt sich durch den großen Aufbau des Choppers der Strahl lediglich in einer Achse vermessen, welche einen kleinen Winkel zur y -Achse einschließt. Die Rekonstruktion des Gauß'schen Strahls macht nur in einem Bereich Sinn, in welchem der Fokus im gemessenen Bereich entlang der optischen Achse liegt. Dies ist der Fall für den gemessenen Eingangsstrahl des Faserkopplers. Durch die Eigenschaften des Gauß'schen Strahls sind die bestimmten Fitwerte für den Strahlradius ω_0 und die Position des Fokus z_0 des Ausgangsstrahls nicht zuverlässig.

Die Vermessung eines Gauß'schen Strahls sollte immer mit der konventionellen Methode durchgeführt werden, um ein zuverlässiges Ergebnis zu erhalten. Die 90/10- und die Chopper-Methode sind für eine grobe Charakterisierung des Strahls ausreichend. Besonders zur groben Bestimmung der Position des Fokus, wodurch die Positionen zur Messung mit der konventionellen Methode sinnvoll gewählt werden kann.

4.2 Outlook

This thesis focuses on a part of an experiment to investigate the sensing of nitric oxide. A three-photon process will be used to excite nitric oxide to a Rydberg state. The ground state $X^2\Pi_{1/2}$ to $A^2\Sigma^+$ transition at 226 nm was investigated in the masters thesis of Fabian Munkes [12]. The setup of this thesis focused on the transition from $A^2\Sigma^+$ to $H^2\Sigma^+$ at 540 nm. The last transition will be realised with light at a wavelength of 835 nm for excitation to a Rydberg state.

The excitation of all three lasers takes place on a gas mixture containing a well known concentration of nitric oxide passing a glass cell. The valence electrons of the excited nitric oxide molecules are then weakly bound and collisions with the background gas will cause ionisation of the molecules. A small voltage applied to the electrodes in the glass cell separate the charges to detect the electron. This signal is amplified for detection. The setup aims to detect nitric oxide down to 5 ppb.

By the time this thesis was handed in, the fiber amplifier was still under repair. Therefore the next step concerning the setup is the optimisation of the optical components for beam shaping customized for the beam of the fiber amplifier. The beam will be focused on the Periodically Poled Lithium Niobate (PPLN) crystal to achieve Second Harmonic Generation (SHG). Following, the characterisation of the PPLN will be accomplished. Additionally, the frequency doubled beam might need to be reshaped for the spectroscopy setup.

Bibliography

- [1] Johannes Schmidt. A trace gas sensor based on rydberg excitations, 2019. URL pi5.uni-stuttgart.de/documents/abgeschlossene-arbeiten/2019-Schmidt-Johannes-A-trace-gas-sensor-based-on-Rydberg-excitations-PhD.pdf.
- [2] Johannes Schmidt. Proof of concept for an optogalvanic gas sensor for no based on rydberg excitation, 2018.
- [3] John V. Zawadzki Robert F. Furchgott. The obligatory role of endothelial cells in the relaxation of arterial smooth muscle by acetylcholine, 1980.
- [4] L.J. Ignarro. Endothelium-derived relaxing factor produced and released from artery and vein is nitric oxide, 1987.
- [5] E.A.Higgs S. Moncada. The discovery of nitric oxide and its role in vascular biology, 2006.
- [6] Ted M. Dawson Hye-Young Yun, Valina L. Dawson. Neurobiology of nitric oxide, 2008.
- [7] Amol Gadbañal S.K.Choudhari, Gokul Sridharan. Nitric oxide and oral cancer: A review, 2012.
- [8] Emel Sayin-Özveri Goncagül Haklar. Different kinds of reactive oxygen and nitrogen species were detected in colon and breast tumors, 2001.
- [9] T. Willems M. Jorissen, L. Lefevere. Nasal nitric oxide, 2001.
- [10] J.M. Lundberg J.O.N.Lundberg, E.Weitzberg. Nitric oxide in exhaled air, 1996.
- [11] Thomas F.Gallagher. *Rydberg Atoms*. Cambridge University Press, 1994. ISBN 978-0-521-38531-2.
- [12] Fabian Munkes. Continuous-wave absorption spectroscopy on the $x^2\pi_{1/2}$ to $a^2\sigma^+$ transition of nitric oxide, 2019.
- [13] D.A.Kleinman. Theory of second harmonic generation of light, 1962.
- [14] D.A.Kleinman G.D.Boyd. Parametric interaction of focused gaussian light beams, 1968.
- [15] Dieter Meschede. *Optik, Licht und Laser*. Vieweg+Teubner, 2008. ISBN 978-3-8351-0143-2.
- [16] Markus Olbrich. Erstellung eines wellenoptischen programms zur berechnung der laserstrahlpropagation nach dem huygens-fresnelschen prinzip, 2010. URL https://monami.hs-mittweida.de/frontdoor/deliver/index/docId/1275/file/Bachelorarbeit_PDF.pdf.

- [17] Robert W Boyd. *Nonlinear Optics*. Elsevir, 2008. ISBN 978-0123694706.
- [18] I.N. Bronstein. *Taschenbuch der Mathematik*. Verlag Europa-Lehrmittel, 10., überarbeitete auflage 2016 edition, 2016. ISBN 978-3-8085-5790-7.
- [19] Orazio Svelto. *Principles of Lasers*. Springer, 4th edition, 1998. ISBN 0-306-45748-2.
- [20] Apache ODETM. The orchestration director engine. URL <https://www.newport.com/n/fiber-optic-coupling>.
- [21] Toptica Photonics. Scientific lasers. URL https://www.toptica.com/fileadmin/Editors_English/11_brochures_datasheets/01_brochures/toptica_BR_Scientific_Lasers.pdf.
- [22] Ee-Leong Lim. High-energy, in-band pumped erbium doped fiber amplifiers, 2012.
- [23] K.S.Abedin. Cladding-pumped erbium-doped multicore fiber amplifier, 2012.
- [24] Covesion. Periodically poled lithium niobate crystal. URL <https://www.covesion.com/assets/downloads/MSHG1080-0.5.pdf>.
- [25] O.Gayer. Temperature and wavelength dependent refractive index equations for mgo-doped congruent and stoichiometric linbo₃, 2008.
- [26] Dieter H. Jundt. Temperature-dependent sellmeier equation for the index of refraction, n_e , in congruent lithium niobate, 1997.
- [27] Stegun Abramowitz. *Handbook of mathematical functions*. Dover Publications, 1964. ISBN 0-486-61272-4.

All links were last followed on Oktober 27, 2019.

Declaration of Authorship

The examination regulations (§27, 7) of the bachelor degree in physics at the university of Stuttgart require the following declaration of authorship.

Ich erkläre hiermit,

1. dass ich diese Arbeit selbständig verfasst habe,
2. dass ich keine anderen als die angegebenen Quellen benutzt und alle wörtlich oder sinngemäß aus anderen Werken übernommenen Aussagen als solche gekennzeichnet habe,
3. dass die eingereichte Arbeit weder vollständig noch in wesentlichen Teilen Gegenstand eines anderen Prüfungsverfahrens gewesen ist, und
4. dass das elektronische Exemplar mit den anderen Exemplaren übereinstimmt.

André Bisquerra
Stuttgart, 30.10.2019

Acknowledgements

At the end of this thesis I would like to thank those who have supported me during my time at the *5th institute of Physics* at the *University of Stuttgart*.

First of all I would like to thank **Prof. Dr. Tilman Pfau** for the opportunity of writing my Bachelor thesis at the *5th institute of Physics*.

I would like to thank to **Dr. Harald Kübler**, **Patrick Kaspar** and **Fabian Munkes** for supervising me during the experimental work in the lab and for the pleasant time in the office as well as reading through my thesis.

Thanks to **Dr. Robert Löw** for the insight into optics during his lecture.

I thank **Dr. Thomas Roessel** for awakening my interest in physics in the first place during my time at the *Werner Siemens Schule Stuttgart*.

I also would like to thank my parents for the constant support during my studies as well as **Manya Willberg** and her parents.

List of Figures

1.1	Schematic waist $\omega(z)$ of a Gaussian beam propagating along the optical z -axis with Rayleigh length z_R , confocal parameter b , curvature $R(z)$ and divergence angle θ	13
1.2	Radial phase of the Gaussian beam dependent on the position along the optical z -axis.	13
1.3	Radius of the Gaussian beam dependent on the position along the optical z -axis.	14
1.4	Phase of the Gaussian beam experiencing a shift in the range of the focus caused by the Gouy phase.	14
1.5	The transversal and longitudinal intensity distribution of a Gaussian beam where the width of the transversal intensity distribution has been expanded for presentation purposes.	15
1.6	Intensity course of the second harmonic along the optical axis for perfect phase matching $\Delta k = 0$ and a phase match missalignment $\Delta k > 1$	20
1.7	Area of normal dispersion in a birefringent material viewing the refractive index for ordinary o and extraordinary e beam polarisation.	21
1.8	Dependency of the refractive index n_e for the extraordinary beam with tilting angle θ of the crystal axes in respect to the optical basis and the refractive indexes n_a and n_c in the basis of the crystal.	21
1.9	Refractive indexes of ordinary and extraordinary beam regarding the tilting angle θ in polar coordinates of a uniaxial material with $n_x < n_y < n_z$ (left) and a biaxial material with $n_x = n_y < n_z$ (right) where the ordinary beam is aligned on the y -axis and the extraordinary beam in the xz -plane.	22
1.10	Lattice and schematic of a periodically poled material with coherence length l_c	23
1.11	Intensity course of the second harmonic along the optical axis for perfect phase matching $\Delta k = 0$, phase match miss alignment $\Delta k > 0$ and quasi phase matching (QPM).	23
1.12	Atom light interaction of a transition between ground $ g\rangle$ and excited $ e\rangle$ state of an atom.	25
1.13	A three level system with a ground state $ 0\rangle$ and two excited states $ 1\rangle$ and $ 2\rangle$	26
2.1	Schematic of the experimental setup of the first part with the optical components described below.	29
2.2	Schematic of the experimental setup with the optical components described below.	30
2.3	Schematic of the working principle of a Polarising Beam Splitter Cube (PBSC).	31
2.4	Schematic of a fiber coupler for a polarisation maintaining single mode fiber with PBSC, focusing lens and fiber mounted on a cage system.	32
2.5	Focusing a gaussian beam onto the Periodically Poled Lithium Niobate crystal.	32
2.6	Schematic of the beam shaping telescope with the focal lengths $f_1 \gg f_2$	33

2.7	Setup scheme of a diode laser with colimating lens and rotatable grating creating an external cavity.	34
2.8	Specifications of the Optical Fiber Amplifier from Keopsys.	34
2.9	Schematic of the periodically poled lithium niobate crystal with different regions of periodicity length Λ provided by the distributor [24].	35
3.1	A picture of the knife edge device used for the measurements. Razorblades are fixed on the xy -stage.	37
3.2	Gaussian profile with 90/10 diameter definition $D_{90/10}$ and D_{1/e^2} relation where the integral from x_{10} to ∞ corresponds to 10% of the total intensity.	40
3.3	A picture of the chopper device used for the measurements.	41
3.4	Conventional knife edge measurement of the beam at the position of the coupler for the fiber amplifier fitted with the error function (3.2).	42
3.5	Waists obtained from the knife edge measurement for different positions z on the optical axis regarding the position of the lens $z_L = 0$ and the waist function (3.4) fitted.	43
3.6	Conventional knife edge measurement at the position where the beam is leaving the coupler for the fiber amplifier with the error fit function (3.2).	44
3.7	Waists obtained from the knife edge measurement for different positions z on the optical axis with regard the position of the lens $z_L = 0$ mm and the waist function (3.4) fitted.	46
3.8	Measured waists with the 90/10 Method of the output beam of the coupler on the optical axis with equation (1.18).	48
3.9	Time dependent signal at the oscilloscope of the beam being cut by the chopper with the rise time and peak width measured by the device.	49
3.10	Measured waists with the Chopper Method of the output beam of the coupler on the optical axis with the fit function (1.18).	51
3.11	Comparison of the different knife edge measurement methods from the obtained data fitted with the fit function (1.18).	52
3.12	Comparison of the different knife edge measurement methods from the obtained data fitted with the fit function (1.18).	52

List of Tables

3.1	Fit parameter of the fit function (3.2) for data sets of the x -axis component. Measured along the optical axis at the position of the input coupler of the fiber amplifier.	42
3.2	Fit parameter of the fit function (3.2) of data sets for the y -axis component. Measured along the optical axis at the position of the input coupler of the fiber amplifier.	43
3.3	Fit parameters of the waist fit function (3.4) for the data sets on x - and y -axis along the optical axis at the position of the coupler for the fiber amplifier and the calculated Rayleigh length z_R from the waist ω_0 with (1.19).	43
3.4	Fit parameter of the fit function (3.2) for the data belonging to the x -axis component along the optical axis of the beam leaving the coupler with regard to the position of the lens $z_L = 0$ mm.	45
3.5	Fit parameter of the fit function (3.2) for the data belonging to the y -axis component along the optical axis of the beam leaving the coupler regarding the position of the lens $z_L = 0$ mm.	45
3.6	Fit parameters of the waist fit function (3.4) for the data sets on x - and y -axis along the optical axis of the beam leaving the coupler regarding the position of the lens $z_L = 0$ mm.	46
3.7	Measured positions of the 10 %, 90 % values of the total power of the knife edge method and the corresponding waist calculated with (3.5) of the x -axis.	47
3.8	Measured positions of the 10 %, 90 % values of the total power of the knife edge method and the corresponding waist calculated with (3.5) of the y -axis.	48
3.9	Fit parameters of the waist fit function (3.4) for the 90/10 measurement on x - and y -axis along the optical axis of the beam leaving the coupler regarding the position of the lens $z_L = 0$ mm.	49
3.10	Measured rise time $T_{\omega,1}$, fall time $T_{\omega,2}$ and peak width T_b with the oscilloscope by cutting the beam and the corresponding waist calculated with (3.7).	50
3.11	Fit parameters of the waist fit function (3.4) for the chopper measurement along the optical axis of the beam leaving the coupler with regard to the position of the lens $z_L = 0$ mm.	50
3.12	Fit parameters of the knife edge measurement methods of the fit function (3.4) for the obtained data along the optical axis of the beam leaving the coupler regarding the position of the lens $z_L = 0$ mm.	51